Nanoscale

Cite this: *Nanoscale*, 2012, **4**, 4348

www.rsc.org/nanoscale

FEATURE ARTICLE

First-principles prediction of charge mobility in carbon and organic nanomaterials

Jinyang Xi, Mengqiu Long, Ling Tang, Dong Wang and Zhigang Shuai*

Received 11th March 2012, Accepted 8th May 2012
DOI: 10.1039/c2nr30585b

We summarize our recent progresses in developing first-principles methods for predicting the intrinsic charge mobility in carbon and organic nanomaterials, within the framework of Boltzmann transport theory and relaxation time approximation. The electron–phonon couplings are described by Bardeen and Shockley's deformation potential theory, namely delocalized electrons scattered by longitudinal acoustic phonons as modeled by uniform lattice dilation. We have applied such methodology to calculating the charge carrier mobilities of graphene and graphdiyne, both sheets and nanoribbons, as well as closely packed organic crystals. The intrinsic charge carrier mobilities for graphene sheet and naphthalene are calculated to be 3×10^5 and $\sim$60 cm^2 V^{-1} s^{-1} respectively at room temperature, in reasonable agreement with previous studies. We also present some new theoretical results for the recently discovered organic electronic materials, diacene-fused thienothiophenes, for which the charge carrier mobilities are predicted to be around 100 cm^2 V^{-1} s^{-1}.

1. Introduction

Organic and carbon nanostructured materials have been intensively studied for their potential applications inorganic solar cells, organic light emitting diodes, organic field-effect transistors and various types of sensors.[1–3] The key factor influencing the performance of these organic electronic devices is the charge carrier mobility, μ, which describes the ability of charge carriers to move in bulk materials. It is defined as $\mu = v/F$, where v is the charge carrier drift velocity and F is the external electric field. Usually, its unit is cm^2 V^{-1} s^{-1}. According to classical mechanics, an electron gains a field-induced momentum $\Delta p = -eF\tau$ during a period of time t. The electron loses its momentum by scattering with lattice vibration, impurities, defects as well as disorders. Therefore, under the steady current condition, we have $\Delta p = -eF\tau$, where τ is the mean scattering time, *i.e.* the average time between two consecutive scattering events. Then the

Key Laboratory of Organic OptoElectronics and Molecular Engineering, Department of Chemistry, Tsinghua University, Beijing 100084, P. R. China. E-mail: zgshuai@tsinghua.edu.cn

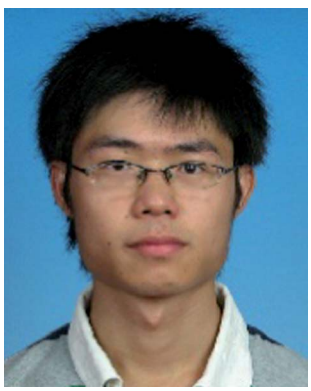

Jinyang Xi

Jin-Yang Xi graduated with a BS degree majoring in physics from Northeast Normal University, Changchun, China in 2009 and is presently a PhD student in Professor Zhigang Shuai's group at Tsinghua University. His research interests are theoretical evaluation of electron–phonon scatterings and charge transport in nanomaterials and molecular crystals.

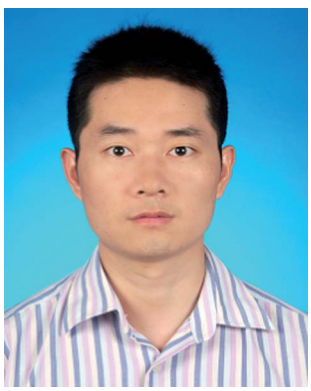

Mengqiu Long

Meng-Qiu Long obtained his PhD in physics supervised by Prof. Keqiu Chen at Hunan University in 2008. He then pursued his postdoctoral research at Tsinghua University on the charge transport properties of nanomaterials based on carbon materials with Professor Zhigang Shuai. In 2010, he joined the faculty of the department of physics, Central South University, Changsha, China, where he is now an associate professor. His current research interests are theoretical modeling of nanomaterials and molecular electronic devices.

velocity of the charge carrier with an effective mass m^* becomes $v = -e\tau F/m^*$. Thus the mobility is expressed as $\mu = -e\tau/m^*$, which suggests that the charge carrier mobility can be improved by increasing the mean scattering time τ or reducing the effective mass m^*. Generally, for traditional inorganic semiconductors, such as silicon single crystal, the mobility is around 10^2 to 10^3 cm^2 V^{-1} s^{-1} at room temperature.[4] Due to its high mobility, as well as natural abundance and stability, silicon is the material by far most widely used in electronic devices. Alternative materials with large high charge carrier mobilities are of great interest and challenging, especially at the nanoscale. Two important milestones in this field are the experimental discoveries of one-dimensional (1D) carbon nanotubes (CNTs) by Iijima[5] and two-dimensional (2D) graphene sheet (GS) by Novoselov *et al.*[6] The mobility of single-walled carbon nanotubes (SWCNTs) can reach 10^4 cm^2 V^{-1} s^{-1} at room temperature,[7] while the mobility of single layer graphene is 10^5 cm^2 V^{-1} s^{-1},[8,9] even reaching 10^7 cm^2 V^{-1} s^{-1} at low temperature.[10] These two carbon materials are considered to be promising for next-generation nanoelectronics. On the other hand, since the first demonstration of thiophene-based field-effect transistors in 1986,[11] organic molecular semiconductors have attracted more and more interest in electronics, opto-electronics as well as printing electronics.[2,12–14] The charge carrier mobilities of organic semiconductors were traditionally low (10^{-5} to 10^{-2} cm^2 V^{-1} s^{-1} at room temperature).[11,15–17] However, since organic materials have great advantages, such as low cost, large area production, easy fabrication, and mechanical flexibility, there have been intensive efforts in recent years through synthesis and processes, to improve their charge carrier mobility and stability. Now, the mobilities of organic materials can reach about 1–10 cm^2 V^{-1} s^{-1} in thin films,[18] and even higher in single crystals of small molecules like rubrene,[19] oligoacenes[20,21] and diacene-fused thienothiophenes (DAcTTs).[22,23] Designing new organic materials with air-stability and large mobilities is a formidable yet promising task.

For more than sixty years, theories to describe charge transport in molecular system have been continuously debated.[24–27] Generally speaking, depending on the electron–phonon coupling strength, three major transport models have been developed,[26,27] *i.e.* fully localized charge hopping model, polaron transport with certain spatial extension, and the fully delocalized band-like mechanisms. The hopping model, at the very beginning, is often employed to describe disordered systems.[28] It assumes that the charge carriers are completely localized and hop from one localized state to another by thermal activation since a higher temperature provides more energy for charge carriers to surpass the energy barriers.[26] Namely, when the intermolecular electron

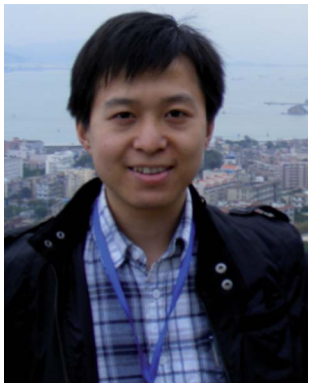

Ling Tang

Ling Tang received his PhD in physics supervised by Prof. Ke Xia at the Institute of Physics of the Chinese Academy of Sciences in 2008. He then moved to Tsinghua University for a postdoctoral stay with Prof. Zhigang Shuai. In 2010 he joined the faculty of the Department of Applied Physics at Zhejiang University of Technology, Hangzhou, China. His main research interests are the first-principles calculations of transport properties in magnetic nanostructures and organic semiconductor materials, including the magnetoresistance in spintronics devices such as spin valves and carrier mobility in pi-conjugated organic crystals.

Dong Wang

Dong Wang received her PhD in physical chemistry supervised by Prof. Qingshi Zhu at the University of Science and Technology of China in 2000. She then worked as a postdoctoral researcher with Prof. Eitan Geva at the University of Michigan, USA, and with Prof. Greg Voth at the University of Utah, USA. Since 2009, she became an associate professor in the Department of Chemistry, Tsinghua University. Her research interests include the theoretical characterization of thermoelectric transport in organic materials and computer simulations of self-assembly in soft matter.

Zhigang Shuai

Zhigang Shuai, PhD 1989 Fudan University, Shanghai. 1990–2001, postdoc and research associate with Prof. Jean-Luc Brédas at the University of Mons, Belgium. 2002–2008, "Hundred-Talent" professor at the Institute of Chemistry of the Chinese Academy of Sciences in Beijing. 2008–date, Changjiang Scholar Chair professor, Tsinghua University, Beijing. His research interests are theoretical modeling of the organic functional materials for the opto-electronic properties. 240 publications with h*-index = 40. Outstanding Young Investigator's Fund (2004) and Chinese Chemical Society-AkzoNobel Chemical Sciences Award (2012). Member of the International Academy of Quantum Molecular Science, the Academia Europaea, and Fellow of the Royal Society of Chemistry.*

coupling (hopping integral V) is much less than the molecular reorganization energy (λ), the charge carrier becomes localized in one single molecule. The hopping model has been popularly described by Marcus theory[29] for many organic materials.[26,30–32] However, for the closely packed molecular single crystals, such as oligoacenes (V is close to or even larger than λ), the transport properties are band-like and the bandwidth can reach a few tenths of an eV,[33] similar to those in inorganic crystals. Several models have been proposed to explain the band-like transport behavior of charge carriers. The first such attempt is the well-delocalized band model, which has been used extensively in inorganic crystals.[33,34] In this model, the electron–phonon coupling is regarded as a perturbation and the charge is delocalized over the crystal. The second is the polaron model, in which the electron is surrounded by phonon clouds, forming a quasi-particle (polaron) due to strong electron–phonon interaction. The polaron model in fact contains both hopping and band mechanisms over different temperature range and due to different electron–phonon coupling strength.[26] The polaron model proposed by Holstein has been well documented in textbooks[35] and the recent developments have been focused on (i) including both local and non-local electron–phonon couplings and considering both inter- and intra-molecular vibrations; (ii) evaluations of parameters from first-principles so that more quantitative studies becomepossible.[36]

Within the polaron model in general, the scatterings by acoustic phonons are usually ignored due to their long wavelength nature. Tang *et al.*[37] have first calculated the mobilities of oligoacenes with acoustic phonon scattering based on Bardeen and Shockley's deformation potential (DP) theory[38] applicable for delocalized charges. Since the hopping and polaron models have been summarized before,[27,39] hereby, we focus on reviewing our recent progresses on applying the band model to charge transport in carbon and organic nanomaterials, including new carbon nanostructures and the tightly packed organic molecular crystals. For the new carbon allotropes, the electron coherence length is close to the acoustic phonon wavelength, and it is much larger than the bond length. For some organic materials, the intermolecular transfer integral is comparable to or even larger than the molecular reorganization energy, the electron transport exhibits band-like behavior.[33,40] In either case it is suitable to deal with the charge transport by the band-like model. Recently, the band model combined with DP theory has been widely applied to charge transport in 1D nanotube,[41] DNA stack[42] and closely packed molecular crystals.[43,44]

Boltzmann transport theory forms the basis for describing charge transport in a weak external field.[35,45] Relaxation-time approximation[45] and the Monte Carlo method[46] have been widely applied to solving the Boltzmann transport equation. The drift-velocity *versus* electric field characteristics can be obtained from Monte Carlo simulation. The slope gives the charge mobility.[47,48] In this work, we focus on the relaxation-time approximation, and describe the computational method will be described in detail in Section 2. According to the Boltzmann transport theory, each time the carriers are scattered elastically by phonons, defects or impurities, the charge distribution function in phase space recovers from drift motion. The scattering rate for the electronic state $(i,\vec{k})$ can be described by the Fermi-golden rule,

$$P_{i\vec{k}} = \sum_{j,\vec{k}'} W\left(ik, j\vec{k}'\right) = \frac{2\pi}{\hbar} \sum_{j,\vec{k}'} \left| M\left(ik, j\vec{k}'\right) \right|^2 \delta\left[\varepsilon_i\left(\vec{k}\right) - \varepsilon_j\left(\vec{k}'\right)\right] \tag{1}$$

Here i,j are the band indexes and $\vec{k},\vec{k}'$ are the electron wavevectors. The matrix element $M(ik,j\vec{k}') = \langle j,\vec{k}'|\Delta V|i,\vec{k}\rangle$ describes the scattering from state $(i,\vec{k})$ to state $(j,\vec{k}')$ by the deviation potential arising from the atomic displacement associated with the phonons or the perturbation potential caused by defects or impurities. Moreover, if we define the electron relaxation-time τ, which is the inverse of the scattering rate, the total electron relaxation-time can be described by Matthiessen's rule

$$\frac{1}{\tau} = \frac{1}{\tau_{ac}} + \frac{1}{\tau_{op}} + \frac{1}{\tau_{imp}} + \cdots \tag{2}$$

which includes contributions from the acoustic phonons τ_{ac}, the optical phonons τ_{op}, the impurities τ_{imp}, as well as others such as piezoelectric scattering,[49] polarity optical phonon scattering[50] and carrier–carrier scattering.[51] The scattering matrix M is the key factor for calculating the charge mobility. A general discussion of different scattering mechanisms in inorganic semiconductors have been described before.[46,52] The impurities and defects are common in the vast majority of materials, and they have a great influence on the charge transport properties, especially at low temperature where phonon effects are minor.[53] Generally, for an ionized impurity in inorganic semiconductors, the scattering source is simply a screened Coulomb potential. There have been two different formulations: the Conwell and Weisskopf approach,[54] where the impurity atom with charge Ze is taken as a naked Coulomb potential $V(r) = \mathrm{Ze}(4\pi\varepsilon\varepsilon_0 r)^{-1}$, and the Brooks and Hering approach,[55] which takes into account the electron screening effect to the potential of the ion, with $V(r) = \exp(-\beta_s r)\mathrm{Ze}(4\pi\varepsilon\varepsilon_0 r)^{-1}$, where $\beta_s = \left(\frac{e^2 n_0}{\varepsilon\varepsilon_0 k_B T}\right)^{1/2}$ is the inverse screening length, n_0 is the free-carrier density. The scattering potential in k-space is determined by the Fourier transformation $\Delta V\left(\vec{k}' - \vec{k}\right) = \Delta V(\vec{q}) = \int V(\vec{r})\exp(-\vec{q}\cdot\vec{r})\mathrm{d}\vec{r}$.[53] Although the impurity and defect scatterings have been studied for more than a half century, a quantitative understanding of electron-impurity (defect) scattering through first-principles calculations has only been possible very recently.[56–58] The screening effect is of vital importance for impurities, and it is often treated by the random-phase approximation.[59–61] The relation between the screened potential and the bare potential at temperature T is determined by $V^{\mathrm{uns}}(\vec{q},T) = \varepsilon(\vec{q},T)V^{\mathrm{scr}}(\vec{q},T)$. The dielectric function is $\varepsilon(\vec{q},T) = 1 + v_c(\vec{q})\Pi(\vec{q},T)$, where $\vec{q} = \vec{k}' - \vec{k}$. $\Pi(\vec{q},T)$ is the irreducible finite temperature polarizability and $v_c(\vec{q})$ is the Fourier coefficient of the electron–electron Coulomb interaction. Hwang and Das Sarma[62] obtained the static polarizability function with the screening effect to explain the transport properties of 2D graphene sheet, while Brey and Fertig[63] have given the scattering rates with screening of scattering potential by free carriers in the graphene nanoribbons. Actually, for organic materials, the impurities and defect states act as traps for the electrons or holes. If its electronic levels are within the band gap, they simply act as a scattering center for the delocalized carriers, just like what discussed above. Although the

defects in molecular semiconductors have been noticed for a long time, the precise nature is still not well understood.[64]

The electron–phonon coupling (EPC) is expressed as $M^{\vec{q}\sigma}_{j\vec{k}\pm\vec{q},i\vec{k}} = \langle j,\vec{k}\pm\vec{q}|\Delta V^{\vec{q}\sigma}|i,\vec{k}\rangle$. $\Delta V^{\vec{q}\sigma}$ is the deviation of the single electron potential with respect to atomic displacement associated with the phonon branch σ with wave vector $\vec{q}$. The EPC has been estimated empirically for both acoustic and optical phonons.[65,66] However, such estimation from transport measurements can give very different results. For instance, the electronic deformation potential constant for graphene has been estimated to range from 10 to50 eV.[67–69] It is desirable to compute EPC at the first-principles level. Following the pioneering work on electron–phonon interaction by Fröhlich,[70] Holstein,[71] Bardeen and Pines,[72] the computational methods developed so far have ranged from frozen-phonon approaches[73–75] to linear response theory.[76–78] For molecular crystals, much work has been devoted to modeling the inter- and intra- electron–phonon couplings based on the hopping or polaron model,[79–82] where the phonon dispersion is often neglected. Recently, a remarkable progress has been made in density functional perturbation theory (DFPT)[83] within the framework of density functional theory (DFT).[84,85] This technique treats phonon $(\vec{q},\sigma)$ as a perturbation to the self-consistent potential created by all electrons and ions. It can significantly reduce the computational time by calculating one primitive unit cell only, instead of constructing a large super cell for the dispersion effect, because it can take into account the phase relation between the neighboring primitive cells. It has been applied to study of the Kohn anomaly and the lattice dynamics,[86–88] superconductormechanism[89] as well as thermoelectric effect.[90] DFPT has been applied with relaxation-time approximation to ionic compounds,[91] the charge mobility in silicon,[56] and monolayer and bilayer graphene.[92,93] But it is still challenging to evaluate the integrals in the first Brillouin zone (BZ) for EPC with high accuracy. For example, in order to compute the electron–phonon scattering rate (eqn (1)), it is necessary to evaluate integrals over all the possible phonon wavevectors (from thousands to millions) in the first BZ. Since the lattice dynamics calculations for each phonon are at least as expensive as the self-consistent field total energy calculation, achieving numerical convergence of integration over the BZ could become a prohibitive computational task. Current calculations are still limited to simple systems with a few atoms per unit cell, and only very few attempts have been made to address complex systems such as metallic nanowires[94] and organic materials.[95] Recently, Louie and coworkers[96] have developed a scheme to exploit the localization character for both electronic and lattice Wannier functions. The electronic and vibrational states and the EPC matrix elements are first calculated in normal Bloch state with few k-points, and then these are transformed into Wannier space. The phonon dynamics matrix and the EPC matrix elements are truncated in Wannier space since they are quite localized, and a generalized Fourier interpolation is applied to back transform EPC matrix to Bloch space with much more dense points in k-space. This technique had been applied to inorganic semiconductors[97,98] and to the potassium-doped picene[99] recently. Because of the computational scaling problem, the calculation of EPC by DFPT may be still unpractical for complex and large systems such as organic materials. For organic and polymeric materials, Vukmirović and Wang[100,101] have developed the charge patching method (CPM), which can be used to calculate the electronic states for systems with tens of thousands atoms, and have calculated EPC of disordered polythiophene bulk materials at first-principles.[102]

In this work, assuming the thermal electron wavelength is close to the acoustic phonon's wavelength, we consider only transport at room temperature and focus on the electron–acoustic phonon coupling in the framework of DP theory,[38] where three major approximations have been assumed: (i) the transverse acoustic (TA) phonon mode is not included due to its negligible effect on the DP;[38](ii) the scattering probability is independent of state momentum; (iii) charge transport direction is assumed to be parallel to the phonon propagation direction.[37] DP theory is coupled with first-principles band structure calculation and the Boltzmann transport theory under the relaxation-time approximation. It was found that this method can well describe the transport properties of various materials, such as carbon[103,104] and organic systems.[37]

This article is structured in the following way. Section 2 describes the theoretical formalism, including Boltzmann transport theory, the DP theory and the effective mass approximation. In Section 3, by taking graphene, graphdiyne, oligoacenes and DAcTTs as examples, we present computational results for the electronic structure and the charge mobility of these materials. Conclusions and outlook are presented in Section 4.

2. Computational methodologies

In this section, we derive the mobility formula based on the Boltzmann transport equation and the relaxation time approximation. The relaxation time can be obtained by applying the deformation potential theory. The effective mass approximation and the first-principles derivation of the parameters in the mobility expression are discussed.

2.1. Boltzmann transport theory

The electron distribution $f_i(\vec{r},\vec{k},t)$ follows the Fermi–Dirac function. It undergoes deformation with an external field and the Boltzmann transport theory assumes that the scatterings restore the distribution function to the original one. Under the steady state condition, we have

$$\frac{\partial f_i\left(\vec{r},\vec{k},t\right)}{\partial t}|_{\text{diff}} + \frac{\partial f_i\left(\vec{r},\vec{k},t\right)}{\partial t}|_{\text{drift}} + \frac{\partial f_i\left(\vec{r},\vec{k},t\right)}{\partial t}|_{\text{scatt}} = 0. \quad (3)$$

If we only consider the weak external direct current (DC) electric field $\left[\frac{\partial f_i\left(\vec{r},\vec{k},t\right)}{\partial t}|_{\text{drift}} = -\dot{\vec{k}}\cdot\frac{\partial f}{\partial \vec{k}} = \frac{e}{\hbar}\vec{E}\cdot\nabla_{\vec{k}} f_i\left(\vec{r},\vec{k},t\right)\right]$, and we ignore the diffusion term, then eqn (3) becomes

$$-\frac{e}{\hbar}\vec{E}\cdot\nabla_{\vec{k}} f_i\left(\vec{k}\right) = \frac{\partial f_i\left(\vec{k}\right)}{\partial t}|_{\text{scatt}}, \quad (4)$$

where $\vec{r},t$ are omitted for simplicity, $\vec{E}$ is the external electric field and i is the band index. The relaxation-time approximation assumes[45]

$$\left.\frac{\partial f_i\left(\vec{k}\right)}{\partial t}\right|_{\text{scatt}} = -\frac{f_i\left(\vec{k}\right) - f_i^0\left(\vec{k}\right)}{\tau_i\left(\vec{k}\right)}, \tag{5}$$

where $f_i^0\left(\vec{k}\right)$ is the equilibrium Fermi–Dirac distribution, while $f_i\left(\vec{k}\right)$ is the local concentration of electron in the state $(i,\vec{k})$ in the neighbourhood of the point $\vec{r}$ in the space and is assumed to deviate not far from $f_i^0\left(\vec{k}\right)$. $\tau_i\left(\vec{k}\right)$ is the relaxation-time from $f_i\left(\vec{k}\right)$ to $f_i^0\left(\vec{k}\right)$ when the external field is removed. Substituting eqn (4) into eqn (5), and neglecting the second-order term, we get

$$f_i\left(\vec{k}\right) \approx f_i^0\left(\vec{k}\right) + e\tau_i\left(\vec{k}\right)\frac{\partial f_i^0\left(\vec{k}\right)}{\partial \varepsilon_i\left(\vec{k}\right)}\vec{E}\cdot\vec{v}_{ik}. \tag{6}$$

By definition, the mobility μ_β is the ratio between the drift velocity $\langle v_\beta \rangle$, and the electric field E_β in the β direction,

$$\mu_\beta^{e(h)} = \frac{\langle v_\beta \rangle}{E_\beta} = \frac{\sum\limits_{i\in \text{CB(VB)}} \int v_\beta\left(i,\vec{k}\right) f_i\left(\vec{k}\right) \mathrm{d}\vec{k}}{E_\beta \sum\limits_{i\in \text{CB(VB)}} \int f_i\left(\vec{k}\right) \mathrm{d}\vec{k}}. \tag{7}$$

The integral in the denominator of eqn (7) for electrons and holes can be expressed as

$$\int f\left(\vec{k}\right)\mathrm{d}\vec{k} \approx \sum_{i\in \text{CB}} \int f_0\left[\varepsilon_i\left(\vec{k}\right) - u\right]\mathrm{d}\vec{k} \tag{8}$$

and

$$\int f\left(\vec{k}\right)\mathrm{d}\vec{k} \approx \sum_{i\in \text{VB}} \int \left\{1 - f_0\left[\varepsilon_i\left(\vec{k}\right) - u\right]\right\}\mathrm{d}\vec{k} \tag{9}$$

where u is the chemical potential. Correspondingly, substituting eqn (6) into eqn (7) and considering that $f_i^0(\vec{k})$ is an even function, while $v_\beta(i,\vec{k})$ is an odd function, and normally the band gap is much larger than $k_\mathrm{B}T$, we can replace the Fermi–Dirac distribution with the Boltzmann distribution. Finally the electron (hole) mobility can be expressed as

$$\mu_\beta^{e(h)} = \frac{e}{k_\mathrm{B}T} \frac{\sum\limits_{i\in \text{CB(VB)}} \int \tau_\beta\left(i,\vec{k}\right) v_\beta^2\left(i,\vec{k}\right) \exp\left[\mp \dfrac{\varepsilon_i\left(\vec{k}\right)}{k_\mathrm{B}T}\right]\mathrm{d}\vec{k}}{\sum\limits_{i\in \text{CB(VB)}} \int \exp\left[\mp \dfrac{\varepsilon_i\left(\vec{k}\right)}{k_\mathrm{B}T}\right]\mathrm{d}\vec{k}} \tag{10}$$

where the minus (plus) sign is for electron (hole). The group velocity $v_\beta(i,\vec{k})$ and band energy $\varepsilon_i(\vec{k})$ can be determined by DFT calculation. The key is to calculate the electron (hole) relaxation-time $\tau_\beta(i,\vec{k})$. The scattering term can be expressed as

$$\left.\frac{\partial f_i\left(\vec{k}\right)}{\partial t}\right|_{\text{scatt}} = \sum_{\vec{k}',j} \begin{Bmatrix} W(j\vec{k}',i\vec{k}) f_j(\vec{k}')[1 - f_i(\vec{k})] \\ -W(i\vec{k},j\vec{k}') f_i(\vec{k})\left[1 - f_j(\vec{k}')\right] \end{Bmatrix} \tag{11}$$

where $W\left(i\vec{k},j\vec{k}'\right)$ is the transition probability from electronic state $\left(i,\vec{k}\right)$ to $\left(j,\vec{k}'\right)$ (see eqn (1)). At the thermal equilibrium,

$$W\left(j\vec{k}',i\vec{k}\right) f_j^0\left(\vec{k}'\right)\left[1 - f_i^0\left(\vec{k}\right)\right]$$

$$= W\left(i\vec{k},j\vec{k}'\right) f_i^0\left(\vec{k}\right)\left[1 - f_j^0\left(\vec{k}'\right)\right].$$

Using Fermi–Dirac distribution, it can be further simplified as:

$$W\left(j\vec{k}',i\vec{k}\right)\exp\left(\varepsilon_i\left(\vec{k}\right)\Big/k_\mathrm{B}T\right)$$

$$= W\left(i\vec{k},j\vec{k}'\right)\exp\left(\varepsilon_j\left(\vec{k}'\right)\Big/k_\mathrm{B}T\right).$$

For elastic scattering $\varepsilon_i(\vec{k}) = \varepsilon_j(\vec{k}')$, we can have $W\left(j\vec{k}',i\vec{k}\right) = W\left(i\vec{k},j\vec{k}'\right)$, thus eqn (11) can be expressed as

$$\left.\frac{\partial f_i\left(\vec{k}\right)}{\partial t}\right|_{\text{scatt}} = \sum_{\vec{k}',j} W\left(i\vec{k},j\vec{k}'\right)\left[f_i\left(\vec{k}'\right) - f_i\left(\vec{k}\right)\right] \tag{12}$$

Combining eqn (1), (5), (6) and (12), the relaxation-time is expressed as

$$\frac{1}{\tau\left(i,\vec{k}\right)} = \frac{2\pi}{\hbar}\sum_{\vec{k}',j}\left|M\left(i\vec{k},j\vec{k}'\right)\right|^2 \delta\left[\varepsilon_i\left(\vec{k}\right) - \varepsilon_j\left(\vec{k}'\right)\right]$$

$$\left[1 - \frac{\tau\left(j,\vec{k}'\right)\vec{v}\left(j,\vec{k}'\right)\cdot\vec{e}_E}{\tau\left(i,\vec{k}\right)\vec{v}\left(i,\vec{k}\right)\cdot\vec{e}_E}\right] \tag{13}$$

where $\vec{e}_E$ is the unit vector along the electric field. In principle, eqn (13) can be solved iteratively. To avoid the iteration, eqn (13) is approximated as

$$\frac{1}{\tau_\beta\left(i,\vec{k}\right)} = \frac{2\pi}{\hbar}\sum_{\vec{k}',j}\left|M\left(i\vec{k},j\vec{k}'\right)\right|^2 \delta\left[\varepsilon_i\left(\vec{k}\right) - \varepsilon_j\left(\vec{k}'\right)\right]$$

$$\left[1 - \frac{v_\beta\left(j,\vec{k}'\right)}{v_\beta\left(i,\vec{k}\right)}\right]. \tag{14}$$

$\left[1 - \dfrac{v_\beta\left(j,\vec{k}'\right)}{v_\beta\left(i,\vec{k}\right)}\right]$ describes the scattering angle weighting factor[105] in the external field direction of β. If we have a spherical energy surface $\varepsilon(\vec{k}) = \hbar^2k^2/(2m^*)$, the weighting factor is $(1 - \cos\theta)$ and θ is the angle between the two wave vectors. Now, the difficulty is to calculate the scattering matrix element. Here we only consider the dominant scattering of a thermal electron or hole by acoustic phonon within the DP theory.

2.2. Deformation potential theory

The DP theory was proposed by Bardeen and Shockley[38] in 1950s to describe the charge transport in non-polar semiconductors. Since the electron velocity with energy $k_\mathrm{B}T$ at 300 K is about 10^7 cm s^{-1}, and the corresponding wavelength is 7 nm, according to $\lambda = h/(mv)$, which is much larger than the lattice constant, thus the electron is scattered mainly by the acoustic phonons.

The DP theory assumes that the lattice potential perturbation due to thermal motions $\Delta V(\vec{r})$ has a linear dependence on the relative volume change $\Delta(\vec{r})$. Namely, $\Delta V(\vec{r}) = E_1\Delta(\vec{r})$, where E_1 is defined as the DP constant. The displacement at site $\vec{r}$ associated with the acoustic phonon with wave-vector $\vec{q}$ is

$$u(\vec{r}) = \frac{1}{\sqrt{N}}\vec{e}_{\vec{q}}\left[a_{\vec{q}}\, e^{i\vec{q}\cdot\vec{r}} + a^*_{\vec{q}} e^{-i\vec{q}\cdot\vec{r}}\right], \tag{15}$$

where N is the number of lattice sites in the unit volume. $\vec{e}_{\vec{q}}$ and $a_{\vec{q}}$ are the unit vector and amplitude of the acoustic phonon $\vec{q}$. The relative volume change can be expressed as

$$\Delta(\vec{r}) \equiv \frac{\partial u(\vec{r})}{\partial \vec{r}} = \frac{i}{\sqrt{N}}\vec{q}\cdot\vec{e}_{\vec{q}}\left[a_{\vec{q}}\, e^{i\vec{q}\cdot\vec{r}} - a^*_{\vec{q}} e^{-i\vec{q}\cdot\vec{r}}\right]. \tag{16}$$

From eqn (16), it is found that only the LA wave contributes to the deformation. So the matrix element for electron (hole) to be scattered from Bloch state $|i,\vec{k}\rangle$ to $|i,\vec{k}'\rangle$ can be expressed as

$$\left|M\left(i\vec{k}, i\vec{k}'\right)\right|^2 = \left|\left\langle i,\vec{k}\left|\Delta V\right|i,\vec{k}'\right\rangle\right|^2 = \frac{1}{N}\left(E_1^i\right)^2 q^2 a_{\vec{q}}^2 \tag{17}$$

where $\vec{q} = \pm(\vec{k}' - \vec{k})$. At high temperature, when the lattice waves are fully excited, the amplitude of the wave is given by $a_{\vec{q}}^2 = k_B T/(2mq^2v_a^2)$ according to the uniform energy partition theory, where m is the total mass of lattice in the unit volume, and $\vec{v}_a$ is the velocity of the acoustic wave. Finally, the average scattering probability becomes

$$\left\langle\left|M\left(i\vec{k}, i\vec{k}'\right)\right|^2\right\rangle = \frac{k_B T\left(E_\beta^i\right)^2}{C_\beta} \tag{18}$$

where $C_\beta = \rho v_a^2 = Nmv_a^2$ is the elastic constant for the longitudinal strain in the direction of propagation of the LA wave (β). E_β^i is the DP constant of the i-th band. We assume that the scattering matrix element is independent of state $\vec{k}$ or $\vec{k}'$, and the charge transport direction (electric field direction) is parallel to the wave vector of LA phonon. The relaxation-time of the LA phonon scattering by DP theory can be expressed as

$$\frac{1}{\tau_\beta\left(i,\vec{k}\right)} = \frac{2\pi k_B T\left(E_\beta^i\right)^2}{\hbar C_\beta}\sum_{\vec{k}'}\delta\left[\varepsilon_i\left(\vec{k}\right) - \varepsilon_i\left(\vec{k}'\right)\right]\left[1 - \frac{v_\beta\left(i,\vec{k}'\right)}{v_\beta\left(i,\vec{k}\right)}\right] \tag{19}$$

Combining eqn (10) and (19), the charge relaxation-time τ and mobility μ can be calculated once the band structure, DP constant E_β^i and the elastic constant C_β are determined.

2.3. Effective mass approximation

Sometimes, the effective mass approximation can be used to simplify the mobility formulae to provide some heuristic insights, though it is not necessary from the first-principles point of view. In the three-dimensional (3D) systems, for the spherical energy surface, the band energy can be written in a very simple form as

$$\varepsilon\left(\vec{k}\right) = \varepsilon_0 + \frac{\hbar^2 k^2}{2m^*}. \tag{20}$$

Here $m^* = \hbar^2/[\partial^2\varepsilon(\vec{k})/\partial\vec{k}^2]$ is the charge effective mass, ε_0 is the energy of band edge. According to eqn (19) and using $(1 - \cos\theta)$ to replace $\left[1 - \frac{v_\beta\left(i,\vec{k}'\right)}{v_\beta\left(i,\vec{k}\right)}\right]$, the relaxation-time τ is

$$\frac{1}{\tau_\beta\left(\vec{k}\right)} = \frac{\sqrt{2\varepsilon_{\vec{k}}}k_B T E_\beta^2 m^{*3/2}}{C_\beta^{3D}\hbar^4\pi}. \tag{21}$$

The mobility of 3D systems is[38]

$$\mu_\beta^{3D} = \frac{e\langle\tau_\beta\rangle}{m^*} = \frac{2\sqrt{2\pi}eC_\beta^{3D}\hbar^4}{3(k_B T)^{3/2}E_\beta^2 m^{*5/2}}. \tag{22}$$

Here $C_\beta^{3D} = \frac{1}{V_0}\frac{\partial^2 E}{\partial(\delta l/l_0)^2}\Big|_{l=l_0}$ is the 3D elastic constant, $\vec{l}_0$ is the lattice vector along the direction of β. Similarly, in the 1D case, the analytical expression of the charge mobility is reformulated by Beleznay *et al.*,[42] and was employed to study the charge transport in the guanine stack,

$$\mu_\beta^{1D} = \frac{e\hbar^2 C_\beta^{1D}}{(2\pi m^* k_B T)^{1/2}E_\beta^2}, \tag{23}$$

where $C_\beta^{1D} = \frac{1}{l_0}\frac{\partial^2 E}{\partial(\partial l/l_0)^2}\Big|_{l=l_0}$ is the 1D elastic constant.

The mobility expression for 2D systems is:[106–108]

$$\mu_\beta^{2D} = \frac{e\hbar^3\rho v_a^2 W_{\text{eff}}}{(m^*)^2 k_B T E_\beta^2} \tag{24}$$

$$W_{\text{eff}} = \left(\int\left|\zeta(z)\right|^4 \mathrm{d}z\right)^{-1}. \tag{25}$$

Here ρ is the mass density of 2D system and v_a is the velocity of the acoustic wave. W_{eff} is the effective width that depends on the degree of carrier confinement in the direction perpendicular to the plane of transport. $\xi(z)$ is an envelope function, which describes the electronic bound state along the direction. For example, in semiconductor layers, such as GaAs/(Ga,Al)As, the energy has a large step at the interface and the layer function is like "infinitely deep square wells". Thus,

$$\xi_n(z) = \left(\frac{2}{L}\right)^{1/2}\sin\left(\frac{n\pi z}{L}\right), \quad (n = 1, 2, 3, \ldots). \tag{26}$$

And $W_{\text{eff}} = 2L/3$, where the layer width (square well width) is L.[108] The eqn (22)–(24) have been employed to study 2D "heterolayer" semiconductors,[107] 2D organic systems,[43] 1D carbon nanotube[109] and graphene nanoribbons.[103] Note that $m^*$is averaged over all directions, which is not appropriate to describe the anisotropic behavior of charge transport and only suitable for the parabolic band. For the example of graphene sheet or the zig-zag graphene nanoribbons, due to the Dirac point or the flat band structure at the Fermi surface, the effective mass approximation fails and one needs to calculate mobility by eqn (10), which includes the detailed information of the band structure and is appropriate to describe the anisotropic transport.

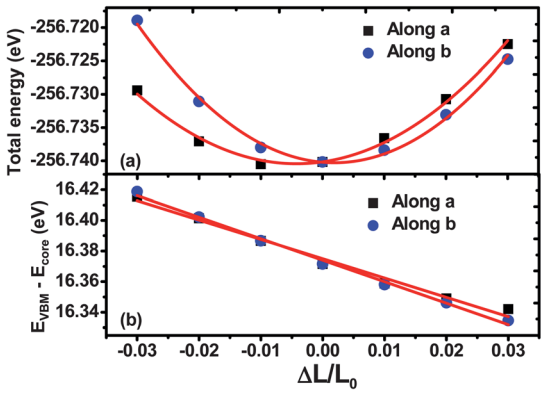

Fig. 1 (a) Total unit cell energy *versus* lattice dilation and (b) band energy of VBM (E_{VBM}) with respect to core level (E_{core}) *versus* lattice dilation. The red lines are the fitting curves. Reproduced from ref. 37 with permission by Science China Press.

2.4. Numerical schemes

To obtain the charge mobility by eqn (10), there are some physical quantities to be determined by electronic structure calculations. Starting with the DFT band structure, we follow Madsen and Singh[110] to apply smoothed Fourier interpolation in k-space in order to obtain denser band. The anisotropic relaxation-time $\tau_\beta(i,\vec{k})$ can be evaluated by eqn (19), with the information of the elastic constant C_β and the DP constant E_β^i. In order to obtain the elastic constant, firstly, we stretch and compress the crystal's lattice vectors along the external field's direction. By fitting the total energy with respect to volume change, $(E-E_0)/V_0$ to dilation $\Delta l/l_0$ with $(E-E_0)/V_0 = C_\beta(\Delta l/l_0)^2/2$, the elastic constant C_β along the transport direction β can be determined. Here V_0 is the cell volume at equilibrium, and l_0 is the lattice constant along direction of β. A typical example of the parabolic fitting of C_β for naphthalene[37] is shown in Fig. 1a. The DP constant is defined as $E_\beta^i = \Delta V_i/(\Delta l/l_0)$, where ΔV_i is the energy change of the i-th band with lattice dilation $\Delta l/l_0$ along the direction of β. In general, we take the energy change at conduction band minimum (CBM) and at valence band maximum (VBM) for electron and hole state, respectively. DP theory that describes the shifts in individual band edges by strain is still under debate.[111–113] This is a serious issue in semiconductor physics because the absolute deformation potential (ADP) is an important factor in assessing quantum confinement for hole or electron in heterostructure quantum wells and nanocrystals.[114,115] The difficulty in theoretical calculation of the ADP is that the absolute position of an energy level with respect to vacuum level in an infinite periodic crystal is ill-defined. The energy of a charged particle is determined by the electrostatic potential where it is located, which in turn depends on the charge density in all space, not just in the local region, owing to the long-range nature of Coulomb interactions. To overcome this problem, here, we follow an approach proposed by Wei and Zunger,[111] which assumed the energy level of the deep core state not sensitive to the slight lattice deformation. Thus, it could be used as a reference to obtain the absolute band edge shifts. The example of linear fitting of E_β^i of naphthalene[37] is shown in Fig. 1b.

Actually, the charge relaxation-time and mobility can be also calculated by effective mass approximation if the energy surface is spherical (isotropic band structure). The effective mass

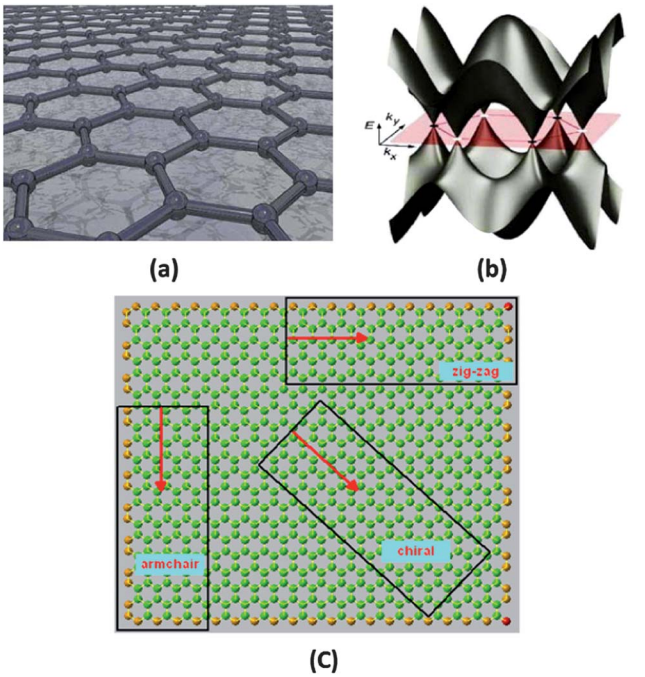

Fig. 2 Schematic presentation of (a) the lattice structure, (b) the band structure and (c) the three nanoribbons building blocks of a single layer graphene.

$m^* = \hbar^2/[\partial^2\varepsilon(\vec{k})/\partial\vec{k}^2]$ can be calculated through a quadratic fit of the energy *versus* k-points for the bottom (top) of CB (VB) for electron (hole).

In the following, the first-principles crystal structure optimization and band structure calculation are carried out using DFT as implemented in Vienna Ab-initio Simulation Package (VASP)[116–119] with a projector augmented wave (PAW)[120] method. The Boltzmann transport equation with relaxation-time approximation is used to calculate the charge mobility eqn (10), and relaxation-time eqn (19) as implemented in the BoltzTraP[110] code, within the DP formalism.

3. Results and discussion

3.1. Graphene

Graphene, a 2D sheet of carbon atoms in a honeycomb lattice (see Fig. 2a), has been found to possess unique electronic properties[121] since its first discovery by Novoselov and Geim *et al.* in 2004.[6] The band structure of the monolayer graphene is shown in Fig. 2b. It is found that the VB and CB only intersect at the k-point (Dirac point) and the energy dispersion is linear. The effective mass of electrons is zero, and the electrons indicate a relativistic-like behavior.[122] This material is very promising in device applications as it has an extremely high intrinsic mobility, which achieves 10^5 cm^2 V^{-1} s^{-1} at room temperature,[8,9] even up to 10^7 cm^2 V^{-1} s^{-1} at $T \leq 50$ K in the decoupled graphene.[10] Three types of 1D graphene nanoribbons (GNRs) can be obtained by cutting graphene along different edges (see Fig. 2c), which include the armchair graphene nanoribbon (AGNR), zig-zag graphene nanoribbon (ZGNR) and chiral graphene nanoribbon (CGNR). Recently, the charge mobility of 1D nanoribbon FETs

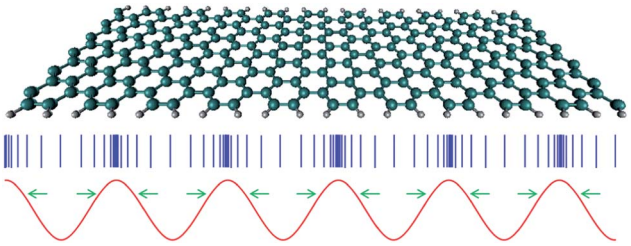

Fig. 3 Schematic presentation of graphene and an acoustic phonon. Reprinted with permission from ref. 103. Copyright 2009 American Chemical Society.

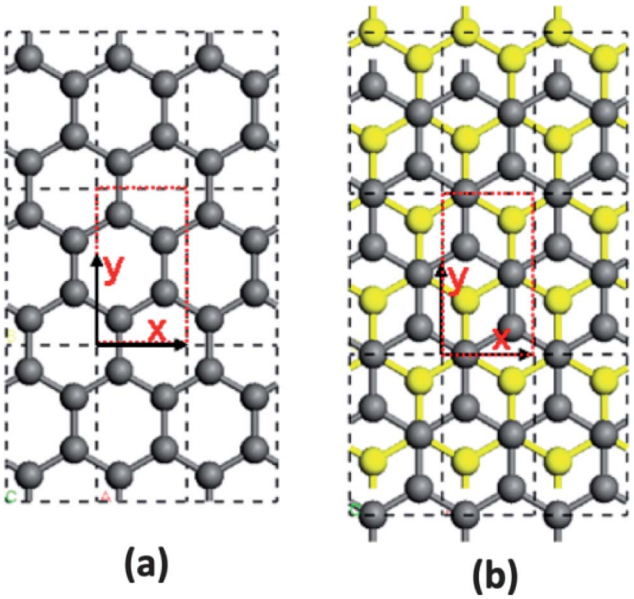

Fig. 4 Schematic representation of (a) single layer graphene and (b) bilayer graphene. The rectangle drawn with red dashed line represents the super cell for transport calculations, and x and y are the transport directions in the plane.

has been found to reach 2700 $cm^2\ V^{-1}\ s^{-1}$,[123] even up to 4900 $cm^2\ V^{-1}\ s^{-1}$ at room temperature.[124] Thus, graphene and GNRs have attracted intensive interests for nanoelectronics of the next generation.[124–128]

Here, we study the charge transport in 2D graphene sheets: single layer graphene (SLG) and bilayer graphene (BLG), as well as 1D GNRs: including AGNRs and ZGNRs. In graphene, which has a covalently bonded conjugated structure, the effective mass is zero and the electron's velocity near the Dirac point is about 10^8 cm s^{-1}.[121,129] Das Sarma *et al.*[121] suggest the equivalent electron de Broglie wavelength can be about 3.5 nm for an unphysically large 2D electron density $n = 10^{14}\ cm^{-2}$. So the electron coherence length is close to the acoustic phonon wavelength and is much longer than the bond length, as show in Fig. 3. And the LA phonon DP theory is used to describe the charge transport in graphene.

3.1.1. Graphene sheets. Two kinds of graphene sheets are discussed, *i.e.*, SLG and BLG, as shown in Fig. 4. The first-principles geometry optimizations and band structure calculations are performed by the PAW method as implemented in VASP. For SLG and 1D nanoribbons, there is only covalently bonded interaction and no intermolecular interaction. Like other authors,[130–132] we employ the Perdew–Burke–Ernzerhof (PBE)[133] generalized gradient approximation (GGA) here. However, there exists non-covalent interaction between the two layers in BLG. Local density approximation (LDA)[85] and PBE have been shown to be poor for description of weak non-covalent interaction.[134] The recently developed PBE-D method[135,136] includes dispersion correction to account for intermolecular interactions. In order to compare the performance of functionals, we use LDA, PBE, and PBE-D methods in the geometry optimization and band structure calculation of BLG. A plane-wave cutoff energy of 600 eV and the total energy convergence criterion of 10^{-4} eV for self-consistent field iteration are used. A $64 \times 64 \times 1$ Monkhorst–Pack[137] k-mesh is chosen. The atomic force converge criterion is 0.005 eV $Å^{-1}$. Vacuum layer thickness is set to be 30 Å.

The PBE optimized interatomic C–C distance is found to be 1.426 Å for SLG, in good agreement with the graphite experiment value 1.422 Å.[138] For BLG, as shown in Table 1, the optimized C–C bond length is always very close to the experimental value no matter what method is used. However, the interlayer distance predicted by PBE shows a large value of 4.167 Å, while the LDA and PBE-D's results are both close to the graphite experimental value of 3.356 Å. Other calculations also show LDA[139] and PBE-D[140] provide quantitative description of the interlayer interaction in BLG.

The calculated band structures of SLG and BLG are shown in Fig. 5. It indicates that both are gapless and the VB and CB intersect at the k-point of the Fermi level. When comparing the band structures near the Fermi level, it is found that both VB and CB of BLG appear in pair and the splittings are small as shown in Fig. 5d. These reproduce well the previous results.[129,141] From Fig. 5d, it can be seen that the band structure calculated by LDA at the optimized geometry is similar to that by PBE-D, but somewhat different from that by PBE near the k-point due to the different interlayer distance optimized by PBE. Min *et al.*[142] have given the band structure similar to that obtained by LDA and PBE-D, calculated by GGA with the experimental structure. Clearly, the difference in the band structure of BLG is caused mainly by the different interlayer distance optimized, not by different functionals used in the calculation. Then, through stretching the lattices along the x and y directions, the elastic constants and the DP constants can be determined. The lattice constants are chosen to be $0.99a_0$, $0.995a_0$, a_0, $1.005a_0$, $1.01a_0$, respectively (while keeping b_0 fixed). According to $C_x^{2D} = \frac{1}{S_0}\frac{a_0^2\partial^2 E}{\partial a^2}|_{a=a_0}$, where $S_0 = a_0b_0$, the elastic constant along the x direction is obtained. Correspondingly, after calculating the band structures at the deformed lattices, the DP

Table 1 The interatomic C–C distances, interlayer distances d and (errors) for BLG, calculated using LDA, PBE and PBE-D methods. The errors are presented in respect with experimental value for graphite (ref. 138)

	Exp.	LDA	PBE	PBE-D
C–C (Å)	1.422	1.415 (−0.007)	1.426 (0.004)	1.426 (0.004)
d (Å)	3.356	3.351 (−0.005)	4.167 (0.811)	3.226 (−0.13)

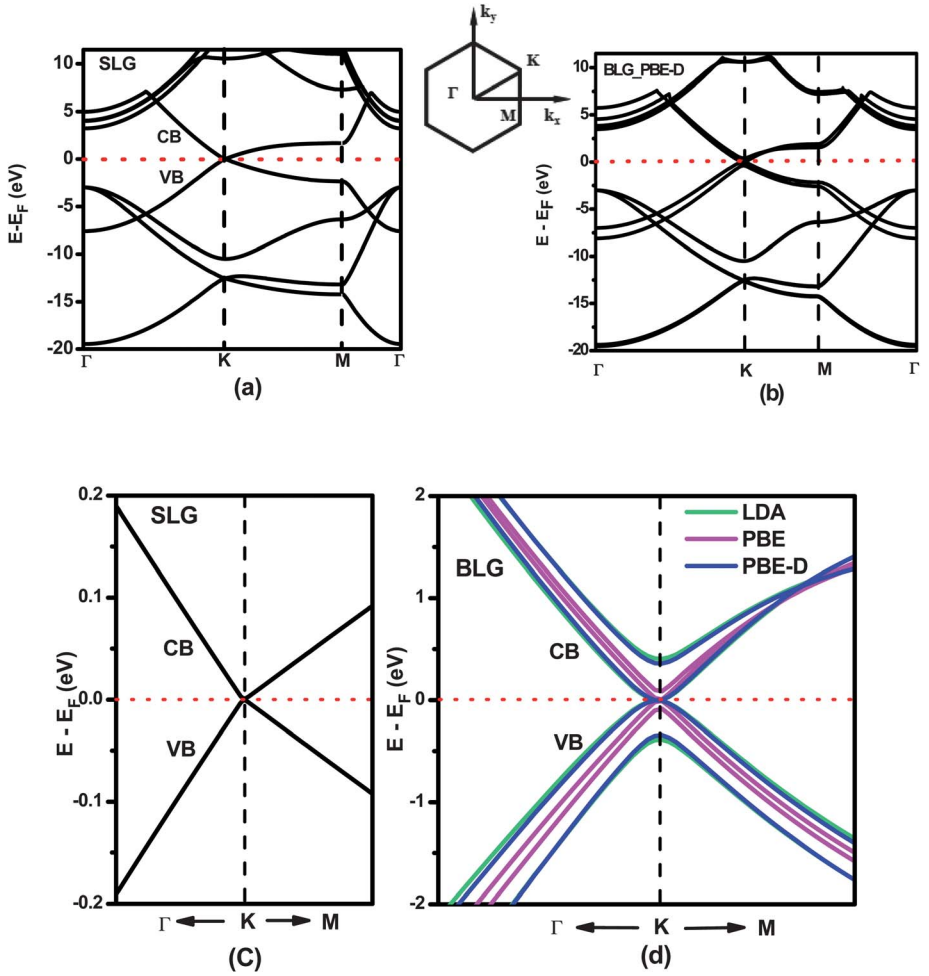

Fig. 5 The band structures of (a) SLG; (b) BLG using PBE-D method; (c) around the Dirac-point k for SLG; (d) Dirac-point k for BLG using LDA, PBE and PBE-D methods, respectively.

constant can be obtained based on the formula $E_1^i = a_0 \partial E/\partial a|_{a=a0}$ (here the i-th band edge is taken as the Fermi level position).

Finally, the charge mobility and the average relaxation time of SLG and BLG are calculated by eqn (10) and (19), respectively. All the relevant results are presented in Table 2. The calculated mobility of SLG is about 3–4 $\times$ 10^5 cm^2 V^{-1} s^{-1} at room temperature that is in good agreement with Geim *et al.*[143], who obtained an experimental value of 4 $\times$ 10^5 cm^2 V^{-1} s^{-1}. Meanwhile, the theoretical electron relaxation time ~13 ps for SLG is close to the experimental value of 20 ps.[10] However, the mobilities calculated for BLG using PBE method (~4 $\times$ 10^5 cm^2 V^{-1} s^{-1}) are somewhat different from those obtained with LDA and PBE-D methods (~10^5 cm^2 V^{-1} s^{-1}), while the LDA and PBE-D results are quite close at 300 K. This difference arises from the fact that the optimized interlayer distance and in turn the band structure by PBE method are different from those by LDA and PBE-D methods. Some experimental studies have indicated that the typical charge mobility in BLG may be much

Table 2 The deformation constant E_1, 2D elastic constant C_{2D}, hole (electron) mobility $\mu\_h(e)$ and hole (electron) relaxation-time $\tau\_h(e)$ for SLG and BLG along directions x and y at 300 K. The calculation of SLG is only studied with the PBE method, while LDA, PBE and PBE-D methods are used to study the transport proprieties of BLG

System	Method	Direction	E_1 (eV)	C_{2D} (J m^{-2})	μ_h (10^5 cm^2 V^{-1} s^{-1})	μ_e (10^5 cm^2 V^{-1} s^{-1})	τ_h (ps)	τ_e (ps)
SLG	PBE	x	5.140	328.019	3.217	3.389	13.804	13.938
		y	5.004	328.296	3.512	3.202	13.094	13.221
BLG	LDA	x	5.276	719.130	0.518	1.294	4.691	10.021
		y	5.537	719.430	0.503	1.104	4.262	9.105
BLG	PBE	x	5.330	680.167	3.949	4.484	16.158	17.966
		y	5.334	681.172	4.178	4.636	16.206	18.019
BLG	PBE-D	x	5.106	774.540	0.452	1.098	4.519	8.116
		y	5.342	804.030	0.475	1.107	4.286	7.697

smaller than that in SLG,[143,144] and recent first-principles calculations have suggested that the lower mobility in BLG may result from the lower electron group velocity and the nonlinear dispersion near the bottom of the conduction band, as well as the substantial differences in EPC in SLG and BLG.[93,145] Borysenko *et al.*[92,93] examined the EPC of SLG and BLG by DFPT, and suggested that the intrinsic scattering mechanism in BLG is dominated by the long-wave acoustic phonon scattering, while the optical phonon scattering is stronger in SLG than in BLG. Based on the evaluation of EPC, they calculated the charge mobilities of SLG and BLG by a full-band Monte Carlo simulation, and the results are 9.5×10^5 cm^2 V^{-1} s^{-1} for SLG and 1.7×10^5 cm^2 V^{-1} s^{-1} for BLG at room temperature. It shows that the charge mobility of SLG is larger than that of BLG by DFPT theory, which is consistent with the experimental findings, and also consistent with our result with LDA or PBE-D functional, but opposite to PBE functional. Overall, the geometry optimization, the band structure and mobility calculation of BLG suggest that LDA can reasonably describe the non-covalent interaction between the two layers, and presents results in good agreement with PBE-D, which takes into account the dispersion correction. Besides, from Table 2, the electron and holes' mobility are close to each other in SLG, while the difference is more pronounced in BLG. This can be attributed to the fact that the interaction between the two sheets influences the curvatures of CB and VB bands.

To summarize, we have discussed the charge mobility of SLG and BLG based on the deformation potential theory, beyond the effective mass approximation. Especially for BLG, three different functionals are compared in order to better describe the non-covalent interaction between layers. The calculated mobility values are in excellent agreement with the experiments of Geim *et al.* as well as with other theoretical results. And we find that LDA can satisfactorily describe the weak intermolecular interaction in BLG. The difference in charge transport in SLG and BLG in our calculations lies in the band structures, namely, the interlayer couplings result in different band curvature as well as in elastic constant, which shed light on understanding the layer thickness dependence of mobility.[146,147]

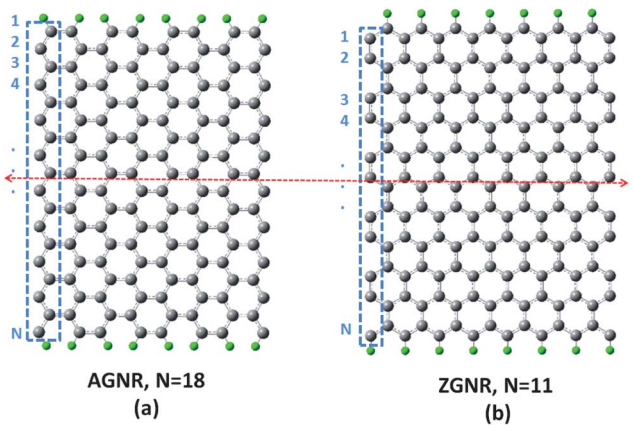

Fig. 6 Schematic representation of (a) armchair ($N = 18$) and (b) zigzag ($N = 11$) edged graphene nanoribbons. The red dashed arrows are the stretching directions.

3.1.2. Graphene nanoribbons. In this part, we are concerned with the size-dependent carrier mobility of graphene nanoribbons AGNRs and ZGNRs, as shown in Fig. 6, where the edge carbons are modeled by hydrogen passivation to avoid any dangling bond. The number of carbon atoms between the two edges, N, represents the ribbon's width. It is our primary interest to know how to cut a graphene sheet to engineer the transport properties[148] from theoretical prediction.[149] Here, the charge mobilities for different ribbon's width of AGNRs and ZGNRs are discussed. We have shown that the width of ribbon plays an important role in tuning the polarity of charge transport.[103]

The geometry optimization and the band structure calculations are carried out using PAW method with PBE exchange correlation functional as implemented in VASP. The energy cutoff is 500 eV and the first Brillouin zone is sampled by $(1 \times 1 \times 200)$ k-points. The structure optimization requests all the atomic forces less than 0.01 eV Å^{-1}. For calculation of mobility, the parameters of effective mass m^* (when appropriate), elastic constant C_{1D} and DP constant $E_1$are determined. The effective mass is calculated by fitting the bottom of CB or the top of VB near the Γ-point. The detailed calculation method of the other parameters is similar to that shown above for graphene in the last part and here we just give the results.

3.1.2.1 Armchair graphene nanoribbon (AGNR). The band structures of AGNRs of $N = 12$, 13, and 14 are shown in Fig. 7. AGNRs are semiconductors with the band gaps of 0.52, 0.88 and 0.15 eV for $N = 12$, 13, and 14, respectively. The relationship the between band gap and ribbon's width $\Delta_{3p} \geq \Delta_{3p+1} > \Delta_{3p+2}(=0)$ (p is a positive integer), proposed by Son and coworkers[150] is satisfied. The band gap of $N = 14$ is calculated to be not zero due to the edge passivation by hydrogen atoms. The band structure of N-AGNRs with $N = 12$ and 13 exhibits a large band gap with a parabolic dispersion around Γ-point and the effective mass is obtained by parabolic fit the band energies within a few k_BT of the band edge. However, with $N = 14$ the band structure shows a small band gap and nonlinear dispersion around the Γ-point. Following Raza and Kan,[151] we examine the band structure of 14-AGNR within a few tens of meV near the Γ-point and find that both VB and CB are parabolic (see Fig. 7b) and the fit is valid for around 10 meV. Thus we simply apply the effective mass approximation eqn (21) here.

To obtain the elastic constant and DP constant, the total energies and band structures at five chosen deformed lattices are calculated: a_0, $0.995a_0$, $1.005a_0$, $1.01a_0$, and $0.99a_0$. The band edge shifts of the CBM and the VBM as a function of lattice dilation for $N = 12$, 13, and 14 are shown in Fig. 8a, for which linear fit is almost perfect. The charge mobilities and relaxation times for AGNRs (N = 9–17, 33–44) are calculated by 1D effective mass approximation formula eqn (23). All the results are collected in Table 3. It is found that (i) electron and hole exhibit very close effective mass in the range $0.057m_0$–$0.077m_0$, comparable to the experimental value of $0.06m_0$ by Novoselov *et al.*[6] where m_0 is the bare mass of electron; (ii) the elastic constant increases with the ribbon's width of AGNRs due to the enhanced rigidity of the system; (iii) relaxation-time is calculated to be several picoseconds as in the graphene sheet, close to the experimental value of 20 ps;[10] (iv) DP constant shows a significant width dependence. It is noted that for $N = 3k$, where k is an

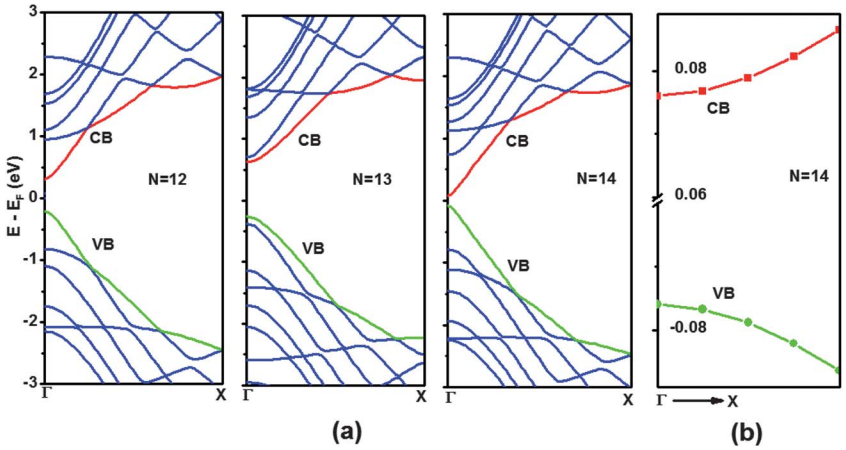

Fig. 7 (a) The band structures of *N*-AGNRs ($N = 12$, 13, and 14) from DFT calculations. (b) The band structure of 14-AGNR, within a few tens meV of the Γ-point. The red and green dashed lines represent the CB and VB, respectively. Reprinted with permission from ref. 103. Copyright 2009 American Chemical Society.

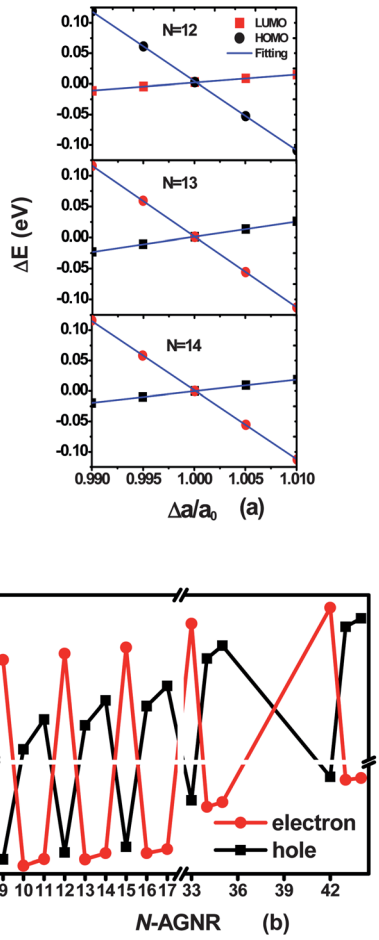

Fig. 8 (a) Band edge shifts as a function of the lattice dilation; (b) hole and electron mobility dependent on the width N of the AGNRs. Reprinted with permission from ref. 103. Copyright 2009 American Chemical Society.

integer, the DP value for hole is about one order of magnitude larger than that for electron, while for $N = 3k + 1$ and $3k + 2$, the situation is just the opposite. According to eqn (23), this gives rise to about two orders of magnitude difference in the mobilities for electrons and holes, see Fig. 8b.

To understand the relationship between DP constant and the ribbon's width, we examine the frontier molecular orbitals at the Γ-point, *i.e.*, the highest occupied molecular orbital (HOMO) for the hole and the lowest unoccupied molecular orbital (LUMO) for electron, see Fig. 9, where the red dashed line stands for the transport direction as well as the stretching direction. For $N = 12$ ($3k$), it is found that the bonding direction of HOMO is perpendicular to the dilation direction and it is of anti-bonding character along the transport direction. While for the LUMO, the bonding direction is along the stretching direction. The bonding state is stable and anti-bonding state is unstable, which means the site energy of anti-bonding state is more prone to change when the structure is deformed. The band-edge shift due to ribbon stretching comes from the site energy change. Thus, DP constant of hole state (HOMO) is larger than that of electron state (LUMO), and hole is scattered more strongly by acoustic phonons than electron. However, for $N = 13$ ($3k + 1$) and $N = 14$ ($3k + 2$) (the $N = 14$ case is not shown in Fig. 9, because it is exactly the same as the $N = 13$ case), the trend is just opposite, and the mobility is much larger for hole than for electron.

3.1.2.2. Zig-zag graphene nanoribbon (ZGNR). The situation for ZGNRs is different from that for AGNRs. From the band structures of ZGNRs ($N = 6$, 7, and 8) (see Fig. 10), it is noted that the CB and VB merge flatly near the Fermi level and ZGNRs are gapless due to the midgap state from the edge. Such band structure excludes the applicability of effective mass approximation. Thus the Boltzmann transport formula eqn (10), instead of eqn (23), is employed. By increasing the ribbon width, it is noted that the mobility change is so small compared with AGNRs and there is no size-dependent carrier polarity charge (see Fig. 11). Besides, the mobility is about two orders of magnitude smaller than that of AGNRs, because ZGNRs exhibits a much smaller bandwidth than AGNRs, and the electron in ZGNRs is more localized. However, the band structure near the Fermi surface can be modulated by doping, and then the mobility can be increased.

Table 3 Calculated width of ribbon W, effective mass m^*, deformational potential constant E_1, the 1D elastic constants C_{1D}, the electron and hole mobility μ, and the averaged value of relaxation-time τ at 300 K for N-AGNRs with $N = 9$–17, 33–35, and 42–44. Reprinted with permission from ref. 103. Copyright 2009 American Chemical Society

N	W (nm)	Carriers	m^* (0.01 m_0)	E_1 (eV)	C_{1D} (10^{11} eV cm^{-1})	μ (10^4 cm^2 V^{-1} s^{-1})	τ (ps)
9	1.176	e	7.21	1.11	3.24	108.11	44.33
		h	6.04	11.00		1.44	0.49
10	1.300	e	7.87	10.992	3.59	1.07	0.48
		h	5.71	2.47		34.30	11.14
11	1.420	e	6.79	10.838	3.81	1.46	0.56
		h	6.51	1.904		50.34	18.63
12	1.543	e	7.17	1.230	4.29	117.36	47.85
		h	6.26	10.904		1.83	0.65
13	1.681	e	7.68	10.972	4.64	1.44	0.63
		h	6.00	2.32		46.71	15.92
14	1.792	e	6.88	10.892	4.84	1.80	0.70
		h	6.65	1.870		64.14	24.26
15	1.913	e	7.23	1.312	5.35	127.26	52.29
		h	6.43	10.960		2.17	0.79
16	2.036	e	7.63	10.954	5.70	1.79	0.78
		h	6.23	2.21		59.74	21.15
17	2.156	e	6.99	11.158	5.87	2.03	0.81
		h	6.81	1.842		77.35	29.96
33	41.19	e	7.02	1.77	12.70	172.835	69.02
		h	6.68	19.2		4.906	1.86
34	42.39	e	7.17	10.84	12.80	4.520	1.84
		h	6.61	2.34		110.072	41.32
35	43.60	e	7.03	18.9	12.98	4.801	1.91
		h	6.88	1.91		130.120	51.8
42	52.24	e	6.94	1.81	17.11	212.163	90.66
		h	6.69	11.19		6.278	2.39
43	53.48	e	7.07	10.96	17.34	6.112	2.46
		h	6.62	2.21		165.953	62.42
44	54.79	e	7.06	10.80	17.45	6.214	2.50
		h	6.70	2.19		185.035	70.8

To conclude, the charge mobility of two different 1D graphene nanoribbons AGNRs and ZGNRs are discussed. The result indicates that: AGNRs exhibit a distinct $3k$ alternating behavior, for $N = 3k$, the electron's acoustic phonon scattering mobility reaches 10^6 cm^2 V^{-1} s^{-1}, while the hole's mobility is 10^4 cm^2 V^{-1} s^{-1}; For $N = 3k + 1$ and $3k + 2$, the hole's mobility is 4–8 $\times$ 10^6 cm^2 V^{-1} s^{-1} and the electron's is about 10^4 cm^2 V^{-1} s^{-1}. However, there is no size-dependent polarity change in ZGNRs.

3.2. Graphdiyne

Carbon allotropes, such as fullerene[152] and carbon nanotubes,[5] have grown as an important research area because of their potentially interesting electronics application in electronics. One new carbon allotrope, graphyne, was theoretically predicted in 1987.[153] After that, efforts have been devoted to chemical synthesis of such a structure, but only some small pieces of graphdiyne have been obtained.[154,155] Only until recently, a large area (~3.6 cm^2) of graphdiyne film has been successfully prepared which was shown to exhibit good semiconducting properties.[156] Fascinating properties including good stability, large third-order nonlinear optical susceptibility, high fluorescence efficiency, high thermal resistance, good conductivity or superconductivity, hydrogen storage, and through-sheet transport of ions have been predicted.[157–161] Graphdiyne is a 2D sheet with one-atom thickness just like graphene, and it contains two acetylenic (diacetylenic) linkages between carbon hexagons,[156] as we can see in Fig. 12.

The charge transport of graphdiyne has been investigated.[104,130] Here, we present the electronic structures and charge mobilities for graphdiyne sheet (GDS) and its 1D nanoribbons (GDRs) based on the Boltzmann transport theory and DP theory.

3.2.1. Graphdiyne sheet (GDNS). The geometry optimization and band structure calculation are carried out using VASP with the PBE functional and the plane-wave cutoff energy is 500 eV. The structural optimization requests the maximum force allowed on each atom is 0.005 eV Å^{-1}. The k-mesh is chosen to be 64 $\times$ 64 $\times$ 1 for the calculations of relaxation time and mobility. The optimized lattice constant is $a_0 = 9.48$ Å, in good agreement with the previous value of 9.44 Å calculated by Narita *et al.*[159] In Fig. 13, a direct band gap of 0.46 eV is found at the Γ-point which means that the graphdiyne sheet is a semiconductor.[153,158] And both the VB and CB are degenerate at Γ-point.

For obtaining the elastic constant and the DP constant, the unit cell is reconstructed to be rectangular (see Fig. 12b). The super cell is dilated along directions of a and b in the range of $\pm$0.1%. The fitting curves are given in Fig. 14. Finally, eqn (10) and (19) are used to calculate the mobility and relaxation time, respectively. The results are listed in Table 4.

The results show that the intrinsic in-plane charge mobilities along directions of a and b are close to each other for both electron and hole. Besides, due to different DP constants for the electron and the hole, it is noticed that electron mobility is about one order of magnitude higher than hole mobility at room

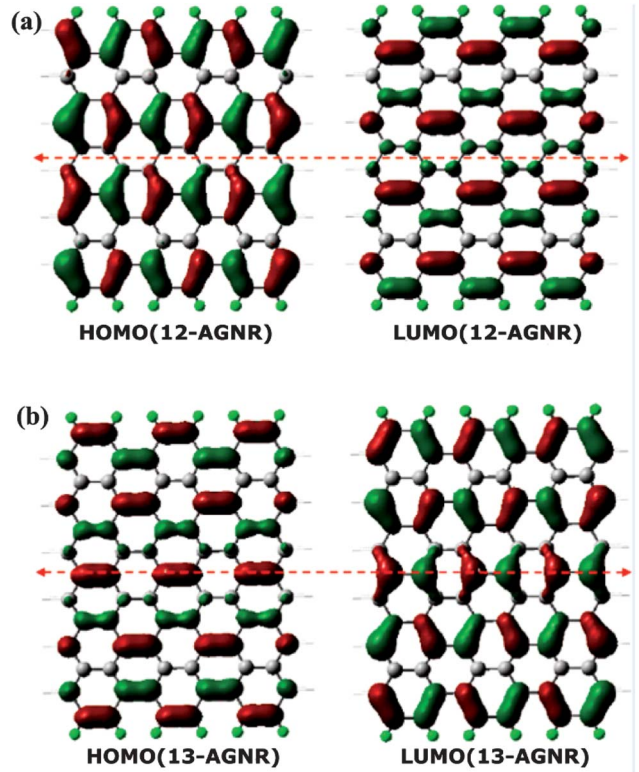

Fig. 9 The Γ-point HOMO and LUMO wave functions for AGNRs with (a) $N = 12$ and (b) $N = 13$. The red dashed line stands for the direction of stretching. Reprinted with permission from ref. 103. Copyright 2009 American Chemical Society.

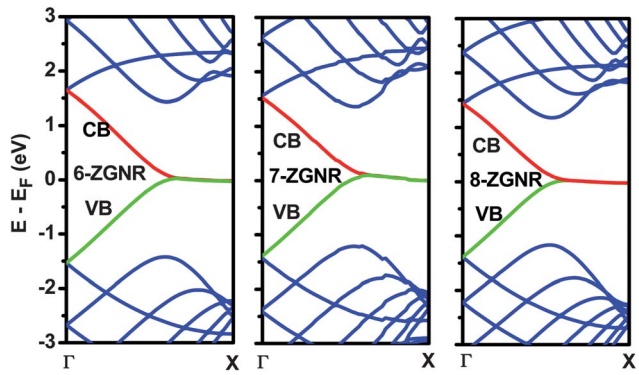

Fig. 10 DFT band structures for N-ZGNRs ($N = 6$, 7, and 8). The red and green dashed lines denote the CB and VB, respectively.

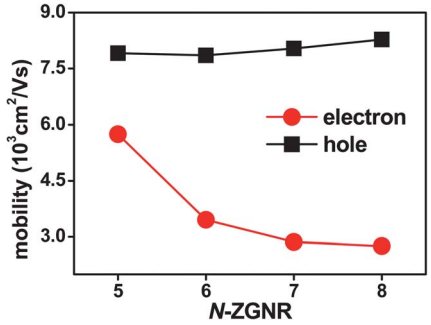

Fig. 11 The hole (electron) mobility for N-ZGNRs calculated as a function of ribbon width N. Reprinted with permission from ref. 103. Copyright 2009 American Chemical Society.

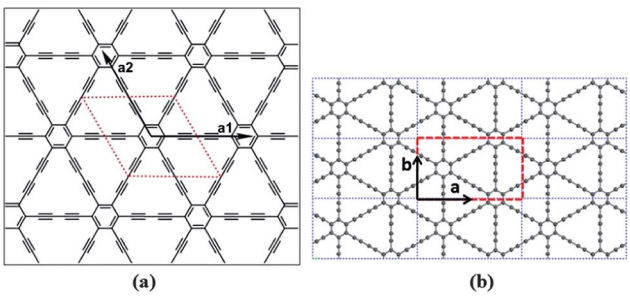

Fig. 12 Schematic representation of a single layer graphdiyne sheet. (a) The rhombus drawn with a red dashed line is the primitive cell for geometry optimization and band structure calculations; (b) the super cell used for transport calculations (dashed rectangle). Reprinted with permission from ref. 104. Copyright 2011 American Chemical Society.

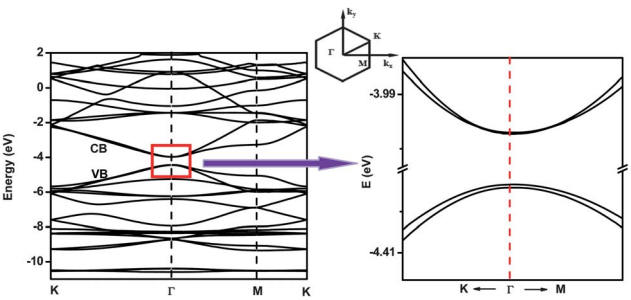

Fig. 13 DFT calculated band structure of a single layer graphdiyne sheet. The CB and VB are both degenerate at Γ-point. The Brillouin zone with the chosen high symmetry k-points is also shown. Reprinted with permission from ref. 104. Copyright 2011 American Chemical Society.

temperature. The DP constant describes the interaction strength of the charge carrier with the acoustic phonon. It indicates that the hole–acoustic phonon interaction is stronger than the electron. It can be understood by checking the frontier molecular orbitals related to transport. Fig. 15 gives the HOMO and LUMO at Γ-point in the directions of a and b. It is found that the HOMO exhibits anti-bonding character between carbon hexagons and diacetylenic linkages whereas the LUMO exhibits bonding feature. Therefore, the hole state shows more nodes than the electron state in both directions a and b. Generally, the band shift upon stretching comes from the site energy change. If an orbital has more nodes in the stretching direction, its energy will be more prone to change against any structural deformation, so that its DP constant is larger. As a result, the DP constant of hole is larger than that of electron in either a or b direction.

Meanwhile, comparing the transport properties of GDS in Table 4 with those of SLG in Table 2, it is found that the calculated mobility of graphene is larger than that of graphdiyne, but both are as high as 10^5 cm^2 V^{-1} s^{-1}, showing that both are excellent low dimensional transport materials. Besides, the GDS's elastic constant is only half of the SLG's, which indicates graphdiyne is more flexible.

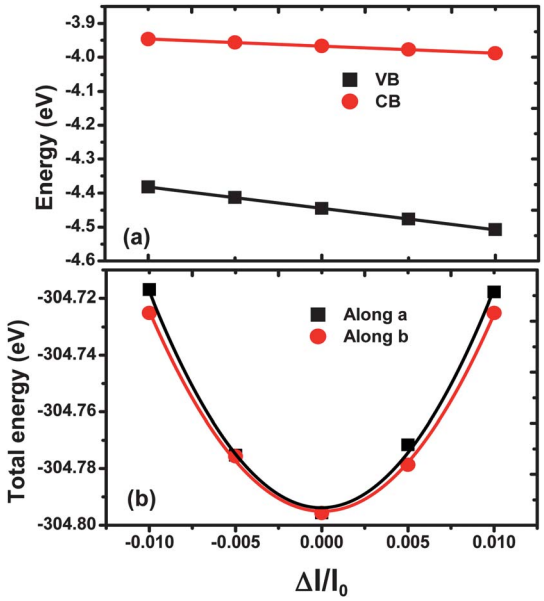

Fig. 14 (a) The band edge shifts of VB and CB with respect to the lattice dilation along the direction of a for the graphdiyne sheet, which give the deformation potential constant; (b) the total energy of a unit cell as a function of lattice deformation along the directions of *a* and *b*, which give the elastic constant. Reprinted with permission from ref. 104. Copyright 2011 American Chemical Society.

Table 4 The calculated deformation potential constant E_1, the 2D elastic constant C_{2D}, the hole (electron) mobility μ, and the averaged value of scattering relaxation-time τ, along the *a* and *b* directions at 300 K for the single layer graphdiyne sheet. Reprinted with permission from ref. 104. Copyright 2011 American Chemical Society

System	Carriers	C_{2D} (J m^{-2})	E_1 (eV)	μ (10^4 cm^2 V^{-1} s^{-1})	τ (ps)
GDS_a	h	158.57	6.30	1.97	1.94
	e		2.09	20.81	19.11
GDS_b	h	144.90	6.11	1.91	1.88
	e		2.19	17.22	15.87

3.2.2. Graphdiyne nanoribbons (GDNRs). In parallel to graphene, we also examine theoretically the 1D graphdiyne nanoribbons. The 2D graphdiyne sheet is cut into various 1D nanoribbons along different edges. Here, five types of GDNRs with different numbers of carbon hexagons between edges are chosen, as shown in Fig. 16, where D1 and D2 are divan-like GDNRs (DGDNRs), Z1, Z2 and Z3 are zigzag GDNRs (ZGDNRs) with different widths. The ribbon widths of these five GDNRs are 12.5 Å, 20.7 Å, 19.2 Å, 28.6 Å and 28.6 Å for D1, D2, Z1, Z2, and Z3 respectively.

The electronic structure and transport parameters are calculated as described before. The charge mobilities are calculated by both Boltzmann transport equations eqn (10) and (19) as well as by 1D effective mass approximation eqn (23). The results are compared in Table 5. The band structures of GDNRs are given in Fig. 17. It shows that the GDNRs are all semiconductors with the smallest band gap of about 0.8 eV for D2.

From Table 5, it is noted that (i) the effective masses of DGDNRs are smaller than those of ZGDNRs, which indicates

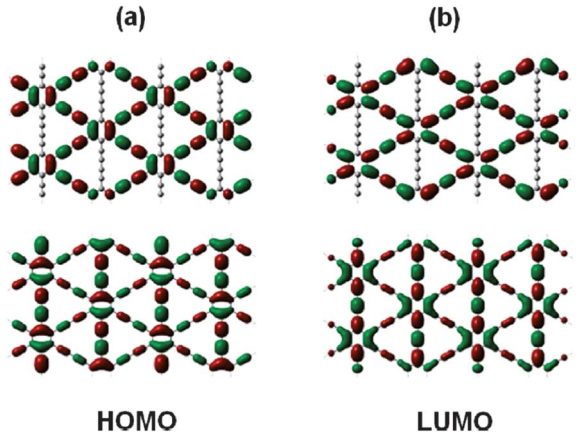

Fig. 15 Γ-Point degenerate HOMO and LUMO density distributions for a singer layer graphdiyne sheet. Note that the number of nodes for HOMO is more than that of LUMO in either direction, which leads to more pronounced scatterings by the longitudinal acoustic phonon for hole than electron. Reprinted with permission from ref. 104. Copyright 2011 American Chemical Society.

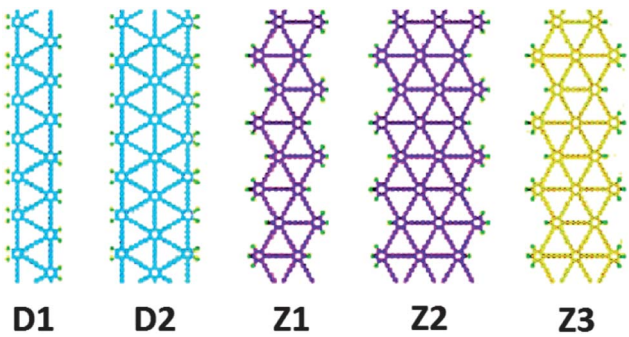

Fig. 16 Schematic representation of five different GDNRs. D1 and D2 are divan GDNRs with two and three carbon hexagons in width respectively. Z1, Z2 and Z3 are zigzag GDNRs with two, three and alternating width, respectively. Reprinted with permission from ref. 104. Copyright 2011 American Chemical Society.

Table 5 Band gap, effective mass (m_h^* and m_e^*), deformation potential constants for VB and CB (E_v and E_c), elastic constant C_{1D}, carrier mobility μ at 300 K for five GDNRs. Note that μ_h and μ_e are comparable with those obtained with the effective mass approximation μ_h^* and μ_e^*. Reprinted with permission from ref. 104. Copyright 2011 American Chemical Society

	D1	D2	Z1	Z2	Z3
Band gap	0.954	0.817	1.205	0.895	1.015
m_h^* (in m_0)	0.086	0.087	0.216	0.149	0.174
m_e^* (in m_0)	0.081	0.086	0.281	0.174	0.207
E_h (eV)	7.406	6.790	4.386	4.786	4.776
E_e (eV)	2.006	1.730	1.972	2.000	2.054
C_{1D} (10^{10} eV cm^{-1})	1.244	1.864	1.035	1.787	1.420
μ_h (10^3 cm^2 V^{-1} s^{-1})	1.696	2.088	0.755	1.815	1.194
μ_e (10^3 cm^2 V^{-1} s^{-1})	18.590	34.241	2.692	9.127	5.329
μ_h^* (10^3 cm^2 V^{-1} s^{-1})	0.711	1.253	0.426	1.073	0.679
μ_e^* (10^3 cm^2 V^{-1} s^{-1})	10.580	19.731	1.418	5.015	2.829

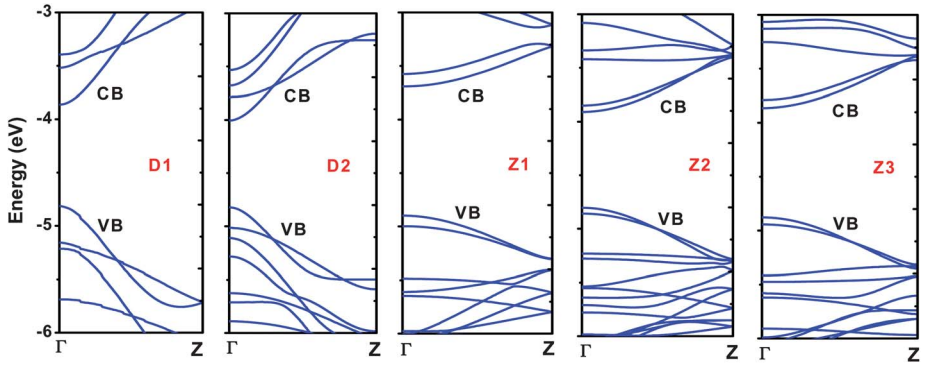

Fig. 17 The calculated band structures of five GDNRs. Reprinted with permission from ref. 104. Copyright 2011 American Chemical Society.

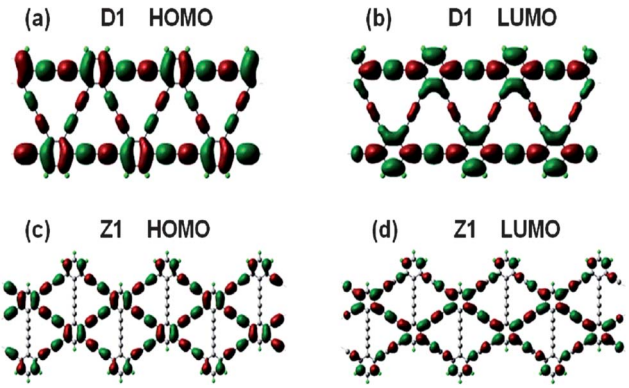

Fig. 18 Γ-Point HOMO and LUMO wave function for GDNRs D1 and Z1. Note that the LUMOs of both D1 and Z1 are more delocalized than those of HOMOs along the horizontal direction, which leads to larger electron mobility than hole. Meanwhile, the LUMO of D1 is more delocalized than that of Z1, suggesting that the electron mobility of D1 is larger than that of Z1. Reprinted with permission from ref. 104. Copyright 2011 American Chemical Society.

DGDNRs have better charge transport properties than ZGDNRs; (ii) the DP constant E_1 for hole is much larger than for electron for all the GDNRs, same as in the graphdiyne sheet. From the frontier molecular orbitals at Γ-point of D1 and Z1, as shown in Fig. 18, the anti-bonding feature between carbon hexagons and diacetylenic linkages has been found for the HOMO, whereas the bonding feature is found for the LUMO. So as explained for GDS, for all GDNRs the hole is more strongly scattered by acoustic phonon than the electron and the intrinsic electron mobility is significantly larger than the hole mobility. Besides, comparing the LUMO of D1 and Z1, the LUMO of D1 is more delocalized in the direction of ribbon axis than that of Z1, this is the reason why mobilities of DGDNRs are all larger than those of ZGDNRs. All of these suggest that DGDNRs are more favorable than the ZGDNRs for the electron transport; (iii) the elastic constant C_{1D} increases with the width of the ribbon. According to eqn (23), the charge mobility increases with the width of the ribbon; (iv) the mobilities from the effective mass approximation eqn (23) are in good agreement with those from the Boltzmann transport formula eqn (10), since the band structure profile is parabolic near the Γ-point.

To summarize this part, the transport properties of the novel carbon allotropes – graphdiyne sheet and its five types of one-dimensional nanoribbons are discussed based on Boltzmann transport theory with the relaxation time approximation and the deformation potential theory. The calculations indicate that the intrinsic charge mobility of the graphdiyne sheet can reach about 10^5 cm^2 V^{-1} s^{-1} at room temperature, which is similar to the graphene sheet. For 1D ribbons, the electron mobility of GDNRs is as high as 10^4 cm^2 V^{-1} s^{-1} at room temperature, which is an order of magnitude higher than the hole. We notice that Bai *et al.*[130] also discussed the charge mobility of 1D GDNRs based on the DP theory and effective mass approach. They calculated two kinds of GDNRs of different widths, with the mobilities in the range of 10^2 to 10^6 cm^2 V^{-1} s^{-1} at room temperature. Besides, they found, independently, that the mobilities of electrons are always larger than those of holes. Our results show, that the charge mobility increases with the ribbon width within the same class of GDNRs, and the mobility of DGDNRs is larger than that of ZGDNRs. It suggests that the charge mobility can be improved and controlled through modulating the graphdiyne nanoribbon's size and edge, just like in graphene nanoribbons. We conclude that the novel carbon nanomaterial graphdiyne is a promising candidate for nanoelectronic engineering and optoelectronic devices.

3.3. Oligoacenes

Usually, due to strong electron–phonon coupling in organic semiconductors, the electron is localized, and the intermolecular electron coupling (V) is much less than the molecular charge reorganization energy (λ). In this case, the small polaron hopping model has been widely employed[39] to investigate the transport mechanism in organic crystals. However, in some closely packed organic crystals, the intermolecular frontier π-orbital overlap is appreciable which leads to band-like transport behavior as in inorganic semiconductors,[40] such as in oligoacenes[33] and DAcTTs.[162] The bandwidth of oligoacenes and DAcTTs can reach about a few hundred meV along the stacked direction[33,43] and the effective masses of electrons in these organic crystals are comparable to the mass of a free electron m_0. For example, in C_{10}-DNTT and C_{12}-BTBT, the effective masses along the lattice vector $\boldsymbol{a}$, are $0.87m_0$ and $1.16m_0$,[43] respectively. So it is reasonable to apply a band model to compute charge carrier mobilities in these systems. In this and the next parts, we only discuss the role of acoustic phonon scattering on the charge transport properties in oligoacenes and DAcTTs with DP theory and Boltzmann

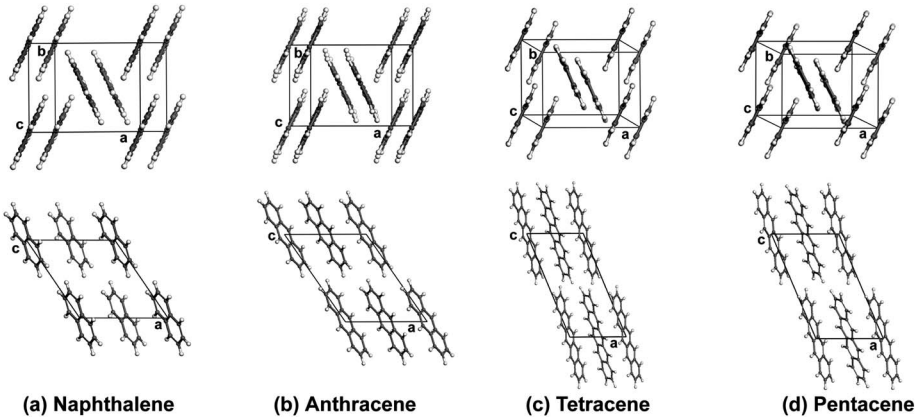

Fig. 19 Crystal structures of oligoacenes: (a) naphthalene, (b) anthracene, (c) tetracene, and (d) pentacene. Reproduced from ref. 37 with permission by Science China Press.

transport theory, while the effect of optical phonon scattering has been completely ignored.

The crystal structures of oligoacenes including naphthalene, anthracene, tetracene, and pentacene, are shown in Fig. 19. It is noticed that there are two molecules in one unit cell and the molecular packing forms herringbone structure.

Though LDA is known to be unsatisfactory for the description of weak intermolecular interactions, some previous reports also suggest that the accuracy of LDA for the π-stacked molecular crystals is reasonable.[163,164] In Section 3.1.1, we have shown that LDA performs well in the description of non-covalent interactions in BLG, and yields the results in good agreement with PBE-D which takes into account the dispersion correction. Therefore, here, LDA is used for the lattice optimization and band structure calculation. The discrepancy in lattice constants between the LDA results and the experimental values[165–167] is within 5%. The plane-wave energy cutoff is 600 eV and the *k*-mesh is chosen to be 8 × 8 × 8 for all the oligoacene crystals in electronic self-consistent calculations. However, this small *k*-mesh is not enough to perform numerical differentiation to obtain the group velocity. Furthermore, the integration in eqn (10) and (19) need much more *k*-points to get converged numerical results. So we need to interpolate the band structure to make a total of 8000 *k*-points in the first Brillouin zone. The band structure and density of states (DOS) of naphthalene are shown in Fig. 20. Naphthalene is an indirect semiconductor, and the band widths of VB and CB are about a few hundred meV. For example, the CB width along *a* direction is 293 meV.

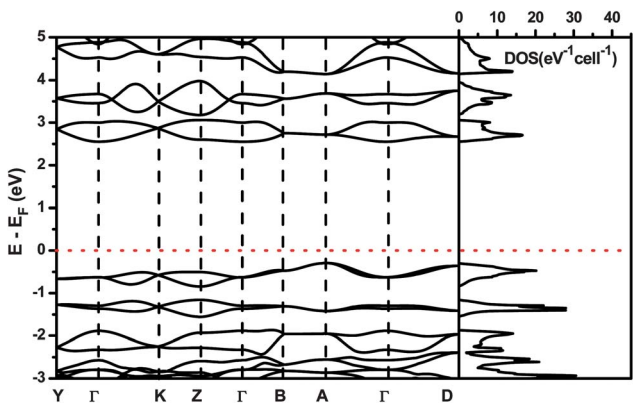

Fig. 20 LDA band structure and DOS of naphthalene. The reciprocal coordinates of high-symmetry points are $\Gamma = (0, 0, 0)$, $Y = (0.5, 0, 0)$, $K = (0.5, 0, 0.5)$, $Z = (0, 0, 0.5)$, $B = (0, 0.5, 0)$, $A = (0.5, 0.5, 0)$, $D = (0.5, 0.5, -0.5)$, respectively. The red dashed line represents the position of the Fermi level.

The fitting procedure as described in Section 2.4 is used to get the elastic constants and DP constants for all the oligoacenes. Only the results along *a* and *b* lattice axes are shown since the in-plane mobilities are dominant. Intrinsic charge mobility is calculated by eqn (10) at room temperature. All the results for oligoacenes are shown in Table 6. It is noted that (i) the elastic constants of naphthalene and anthracene are close to each other and same applies, for tetracene and pentacene. The elastic constants along the *b* direction are larger than those along the *a* direction, which is in qualitative agreement with the experimental results;[168] (ii) DP constants of the hole are larger than those of the electron, suggesting that the hole scattering by LA phonon is stronger than the electron; (iii) the molecular length dependency of mobility is masked by different crystal packing modes. The hole mobilities are found to be about a few tens of cm^2 V^{-1} s^{-1}, for example, naphthalene's mobility is around 50.4–74.4 cm^2 V^{-1} s^{-1} at room temperature. These values are three times smaller than those obtained by Wang *et al.*,[36] based on the Holstein–Peierls model and electron–optical phonon coupling only, where the hole mobility of naphthalene was found to be around 150–200 cm^2 V^{-1} s^{-1}. It may suggest that the acoustic phonon scattering cannot be neglected in the charge transport of these molecule crystals; (iv) the experimental mobility of oligoacene is about1 cm^2 V^{-1} s^{-1} at room temperature,[169–171] which is much smaller than our calculation. This might be attributed to the impurities or defects in materials. The hole mobility of ultrapure pentacene single crystal is reported to be 35 cm^2 V^{-1} s^{-1} at room temperature,[21] which is in good agreement with our result. (v) Most organic semiconductors are hole transport (p-type) materials, because the injected charges are mostly holes and inherently, there are much more electron traps than hole traps in organic materials. But our theoretical results indicate that for anthracene (*a* direction) and pentacene (*b* direction), the electron mobility can be as high as more than

Table 6 Calculated elastic constant C_{3D}, hole (electron) deformation potential constant E_1 and the hole (electron) mobility μ for oligoacenes along lattice directions *a* and *b* at 300 K

	Naphthalene	Anthracene	Tetracene	Pentacene
C_a (10^9 N m^{-2})	16.24	16.36	13.80	14.45
C_b (10^9 N m^{-2})	21.10	19.93	19.86	19.83
E_a^h (eV)	1.31	1.12	1.79	2.10
E_a^e (eV)	1.39	1.38	0.47	0.79
E_b^h (eV)	0.96	0.42	1.60	1.81
E_b^e (eV)	0.56	0.87	0.53	0.38
μ_a^h (cm^2 V^{-1} s^{-1})	50.4	19.2	10.6	15.2
μ_a^e (cm^2 V^{-1} s^{-1})	39.8	245	24.5	27.7
μ_b^h (cm^2 V^{-1} s^{-1})	74.4	42.2	92.5	55.6
μ_b^e (cm^2 V^{-1} s^{-1})	35.3	15.4	87.6	295

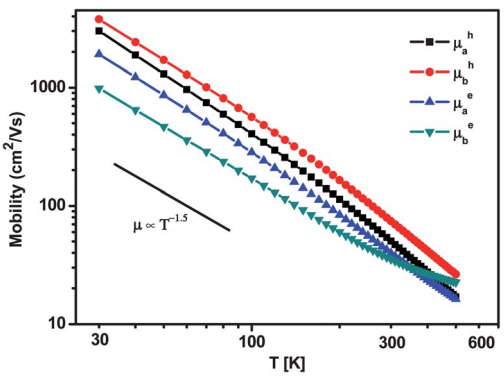

Fig. 21 Temperature dependence of hole and electron mobilities along *a* and *b* directions for naphthalene. The power law with factor −1.5 is shown in the figure which describes the temperature dependence of charge carrier mobility with the effective mass approximation. Reproduced from ref. 37 with permission by Science China Press.

two hundred cm^2 V^{-1} s^{-1} due to the much smaller DP constant and small "effective mass" as shown in Table 6.

The temperature-dependent hole and electron mobilities of electron and hole along the *a* and *b* directions of naphthalene is depicted in Fig. 21. The temperature effect arises from the distribution function in eqn (10) and the mobility manifests a typical power law temperature dependence, owing to the assumption of band transport mechanism in DP theory. The calculated temperature dependence can be approximated as $\mu \propto T^{-1.5}$, as manifested in the effective mass approximation eqn (22).

3.4. Diacene-fused thienothiophenes (DAcTTs)

Newly discovered diacene-fused thienothiophenes (DAcTTs)[162] have been demonstrated to possess high mobility and air stability.[22,23,172–175] For example, for 2,7-dioctyl[1]benzothieno[3,2-*b*][1]benzothiophene (C_8-BTBT, Fig. 22), the hole mobility has been shown to be as high as 31 cm^2 V^{-1} s^{-1} from solution process.[23,172,173] It is suggested that the intermolecular hydrophobic interaction between alkyl chains effectively enhances intermolecular interaction in the BTBT core layers, favoring charge transport. DAcTTs have been found to exhibit a band-like transport property. Temperature-dependent Hall-effect measurements of 2,9-didecyl-dinaphtho[2,3-*b*:2′,3′-*f*]thieno[3,2-*b*]thiophene (C_{10}-DNTT) solution-crystallized OFET indicate that the mobility increases with decreasing temperature.[22] Theoretical calculations showed that DAcTTs have a low-lying HOMO energy level, 5.58 eV for BTBT and 5.18 eV for DNTT, favoring air stability. The hole's reorganization energy of dianthra[2,3-*b*:20,30-*f*]thieno[3,2-*b*]thiophene (DATT) is calculated to be 86 meV, which is smaller than that of pentacene (94 meV). Besides, the herringbone packing structure could enhance the intermolecular coupling, such as in DATT, with charge transfer integral to be 88 meV for HOMO.[176] The high charge mobilities can be attributed to strong electronic coupling interaction between neighbouring molecules and small intramolecular reorganization energy.[30,177] Here, we investigate the charge transport in DAcTTs, *i.e.* C_8-BTBT, DNTT and DATT, with molecular structure shown in Fig. 23, by employing the acoustic phonon DP theory model and Boltzmann transport theory with relaxation time approximation at first-principles level.

The geometric optimization and band structure calculation are performed by DFT with the LDA functional in the VASP package. The lattice constants and the atomic coordinates have been determined by X-ray diffraction by Takimiya *et al.*,[173,176,178] and are further optimized by DFT. The structural optimization is done with the maximum force allowed on each atom being 0.01 eV Å^{-1} and the plane-wave energy cutoff of 600 eV. For

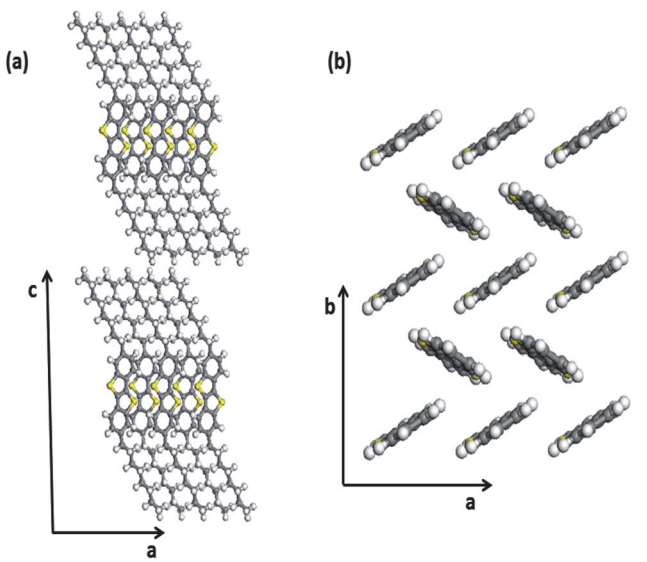

Fig. 22 The crystal structure of C_8-BTBT, (a) *a*–*c* plane and (b) *a*–*b* plane.

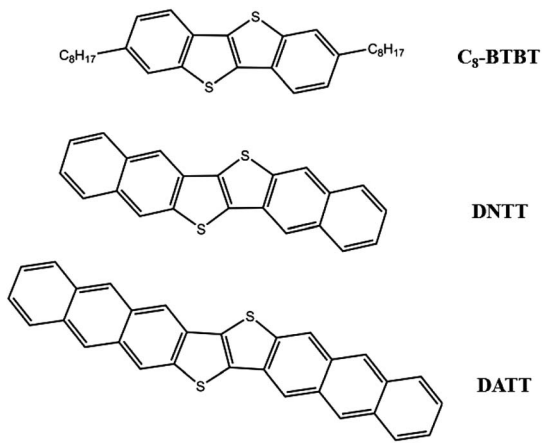

Fig. 23 The chemical structures of diacene-fused thienothiophenes (DAcTTs): C_8-BTBT, DNTT and DATT.

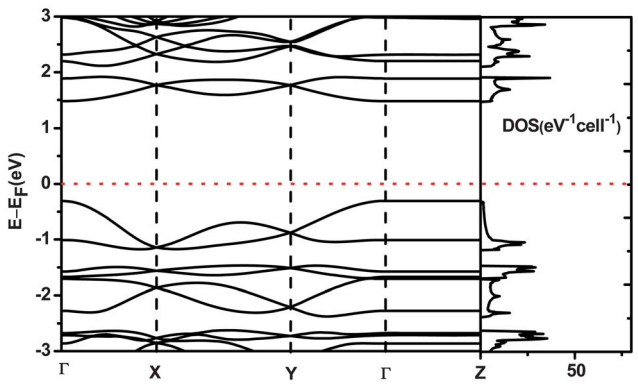

Fig. 24 The DFT-calculated band structure and DOS of C_8-BTBT. The reciprocal coordinates of the high-symmetry points are $\Gamma = (0\ 0\ 0)$, $X = (0.5\ 0\ 0)$, $Y = (0\ 0.5\ 0)$ and $Z = (0\ 0\ 0.5)$, respectively. The red dashed line is the position of the Fermi level.

C_8-BTBT, the SCF calculation has been done with $10 \times 10 \times 1$ grid in k-space and the band structure along the high symmetry line and DOS are shown in Fig. 24. It is found that C_8-BTBT is a direct band-gap semiconductor. Meanwhile C_8-BTBT exhibits a very large bandwidth, 0.84 eV for VB along the a direction. The bandwidths of both VB and CB along c direction are both exactly zero. To check this result, we redo a SCF calculation with $10 \times 10 \times 4$ k-mesh and the band structure calculation. It demonstrates that along c direction, the bandwidths of both VB and CB are both nearly zero (10^{-5} eV). So, C_8-BTBT is expected to exhibit 2D transport behavior. We can also understand this from the lattice structure: the long alkyl chain makes the electronic coupling to neighboring molecule in the c dimension extremely weak and charge carriers are confined within a single molecular layer. Both DNTT and DATT are indirect band-gap semiconductors, with valence bandwidths being 0.33 eV and 0.20 eV respectively in the a direction, respectively. The bandwidths of the VB and CB of these three systems in a and b directions are given in Table 7 for these three systems. The results show that the herringbone packing structure leads to large intermolecular interaction, suggesting band-like transport

Table 7 The calculated VB (CB) W, elastic constant C, hole (electron) deformation potential constant E and the hole (electron) mobility μ for DAcTTs along a and b directions at 300 K

	C_8-BTBT	DNTT	DATT
W_a^h (eV)	0.84	0.33	0.20
W_a^e (eV)	0.29	0.16	0.15
W_b^h (eV)	0.57	0.24	0.17
W_b^e (eV)	0.29	0.20	0.24
C_a (10^9 N m^{-2})	20.51	18.6	19.3
C_b (10^9 N m^{-2})	15.53	13.2	14.3
E_a^h (eV)	1.65	1.76	1.99
E_a^e (eV)	2.64	0.39	0.56
E_b^h (eV)	3.55	0.97	0.46
E_b^e (eV)	1.13	0.57	0.76

mechanism. To calculate the DP constant E_1 and the elastic constant C, the lattice constants are stretched up to 3% (only a and b directions are considered). For example, the band structures and the total energies at $0.97a_0$, $0.98a_0$, $0.99a_0$, a_0, $1.01a_0$, $1.02a_0$, and $1.03a_0$ are calculated. The band edge positions of the VB and CB as a function of the dilation along a is shown in Fig. 25a, and the total energy as a function of the dilation along directions of a and b are presented in Fig. 25b. The elastic constant C is fitted by $(E - E_0)/V_0 = C(\Delta l/l_0)^2/2$. The DP constants and the elastic constants of C_8-BTBT, DNTT and DATT are also given in Table 7. Finally, according to eqn (10), the charge mobilities of C_8-BTBT, DNTT and DATT are calculated, which are given in Table 8. We also include some experimental and other theoretical mobility values of these materials in Table 8 for comparison.

From Tables 7 and 8, we find that (i) the bandwidths of these materials are all very large, about a few hundred meV. Especially for C_8-BTBT, the bandwidth of VB along the a direction reaches 0.84 eV because of the stronger intermolecular interaction caused by the alkyl chain. The alkyl chain can enhance the

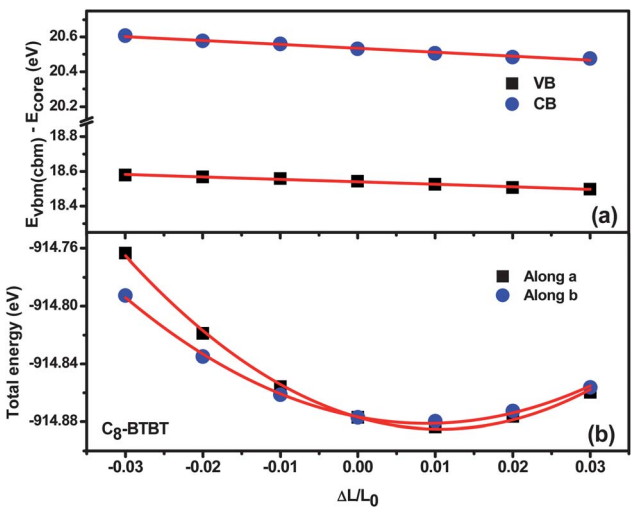

Fig. 25 (a) The band energy of VBM (E_{VBM}) and CBM (E_{CBM}) with respect to the core level (E_{core}) with uniform dilation along a direction for C_8-BTBT; (b) the total energy of a unit cell as a function of lattice deformation along a and b directions for C_8-BTBT with parabolic fitting.

Table 8 The calculated electron (hole) mobility μ for DAcTTs along *a* and *b* directions at 300 K and mobilities of these materials reported by others. The experimental results show $\mu_{C8\text{-}BTBT} > \mu_{DATT} > \mu_{DNTT}$ and our results of hole mobility are in qualitative agreement with experimental ones

	C_8-BTBT	DNTT	DATT
μ_a^h ($cm^2\ V^{-1}\ s^{-1}$)	609.0	76.4	19.1
μ_a^e ($cm^2\ V^{-1}\ s^{-1}$)	12.3	164.7	107.6
μ_b^h ($cm^2\ V^{-1}\ s^{-1}$)	86	137.7	322.6
μ_b^e ($cm^2\ V^{-1}\ s^{-1}$)	77.5	91.5	90.8
μ ($cm^2\ V^{-1}\ s^{-1}$)	9.1 (ref. 172)[a]	8.3 (ref. 175)[a]	16 (ref. 30)[a]
	31 (ref. 23)[a]	1.9 (ref. 30)[b]	3.14 (ref. 30)[b]

[a] The mobility of the single crystal based OFETs in experiments at 300 K. [b] The mobility from theoretical calculation based on the Marcus theory of charge transfer rates at 300 K.

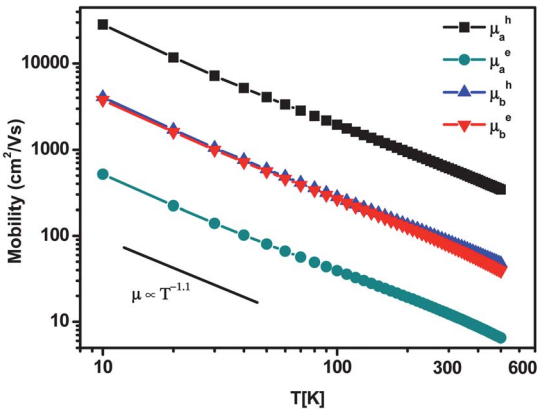

Fig. 26 Temperature dependence of hole and electron mobilities along *a* and *b* directions for C_8-BTBT. The power law with a factor −1.1 is shown in the figure indicating a 2D transport behavior.

intermolecular interaction in BTBT. The experiments do support such observation: for unsubstituted-DNTT,[175] charge mobility has been measured to be 8.3 $cm^2\ V^{-1}\ s^{-1}$ and for the alkylated-DNTT,[22] it becomes 12 $cm^2\ V^{-1}\ s^{-1}$; (ii) due to the large bandwidth and small DP constant, the charge mobilities of the three DAcTTs are all very high, some directions of electron or hole mobilities are even higher than a few hundred $cm^2\ V^{-1}\ s^{-1}$ at room temperature. For the hole mobility, the largest one is C_8-BTBT along the *a* direction (609 $cm^2\ V^{-1}\ s^{-1}$), the second largest is DATT along the *b* direction (322.6 $cm^2\ V^{-1}\ s^{-1}$), and the lowest is DNTT along the *b* direction (137.7 $cm^2\ V^{-1}\ s^{-1}$). Our theoretical results agree with experimental ones in trend as showed in Table 8. However, the theoretical values are much larger than the experimental ones. Such a discrepancy might be due to the following reasons: (a) the materials used in the experiment are solution processed film, instead of ultrapure single crystals as in oligoacenes; (b) here we have only considered the acoustic phonon scattering and neglected scatterings by the optical phonons, as well as the impurities and defects scatterings, which are the dominant scattering mechanism in real systems; (iii) comparing DAcTTs with oligoacenes, we find that the hole mobility of DAcTTs is usually larger than those of oligoacenes in the direction of lattice vectors. Theoretically, the intermolecular interaction is the key to the mobility and its strength depends on many factors, mainly on the intermolecular geometry. The mobility of DAcTTs and oligoacenes investigated here are all in the direction of crystallographic *a* and *b* axes, the so-called edge-to-edge pair type. However, compared to the direction of (110) and ($\bar{1}$10), the so-called edge-to-face pair type, the intermolecular interactions in oligoacenes in the edge-to-edge pair is smaller because of less effective intermolecular contact in the *a* and *b* directions.[179,180] For DAcTTs, in the case of the edge-to-edge pair type, the sulfur atoms can effectively interact intermolecularly and the large HOMO coefficients on the sulfur atoms also contribute to increase intermolecular overlap. These lead to larger intermolecular interactions in DAcTTs than oligoacenes in the *a* and *b* directions.[162] For example, the largest transfer integrals of HOMOs in the crystallographic *a* direction of DATT and DNTT are 70 meV and 71 meV by DFT calculations,[176] while those of the naphthalene and pentacene are 35.6 meV and 33.8 meV, respectively.[179] So DAcTTs exhibit better transport properties in these directions.

Finally, the temperature dependence of hole and electron mobilities along directions *a* and *b* for C_8-BTBT is depicted in Fig. 26. The temperature effect arises from the distribution function in eqn (10) which manifests the typical power law behavior, due to the intrinsic band transport mechanism in DP theory. The temperature dependence can be approximated as $\mu \propto T^{-1.1}$, manifesting a 2D transport behavior, see eqn (24). The result is in good agreement with the above analysis of the band structure of C_8-BTBT. However, the temperature-dependent mobility of naphthalene (see Fig. 21) exhibits a 3D transport behavior with power factor of −1.5. This difference is due to different bandwidths along the *c* direction. The bandwidths of VB and CB for naphthalene are 0.064 eV and 0.048 eV, respectively (see Fig. 20), while they are nearly zero for C_8-BTBT. Therefore the two materials show different transport behaviors according to eqn (10). From the lattice structure, the long alkyl chain of C_8-BTBT makes the electronic coupling to neighboring molecule extremely weak in the *c* dimension and charge carriers are confined within a single molecular layer, which is not the case in naphthalene.

In summary, using Boltzmann transport theory and the DP theory coupled with first-principles calculations, we have investigated the intrinsic charge mobility of three DAcTTs compounds: C_8-BTBT, DNTT and DATT, which have recently been demonstrated with excellent charge transport property. Our results of hole mobility show $\mu_{C8\text{-}BTBT} > \mu_{DATT} > \mu_{DNTT}$ at 300 K and this observation is in qualitatively agreement with experiments and other theoretical calculations. Due to the alkyl chains' enhanced intermolecular interaction, C_8-BTBT exhibits a large bandwidth of 0.84 eV and a high hole mobility of 609 $cm^2\ V^{-1}\ s^{-1}$. Besides, the temperature dependence of mobility of C_8-BTBT shows a 2D transport behavior, which is different from that of oligoacenes.

From the discussion of charge transport in oligoacenes and DAcTTs, it suggests that the current treatment only acoustic phonon scattering is taken into account, while the effect of optical phonon scattering has been completely ignored, which can cause overestimation of mobilities. In comparison with new carbon allotropes like graphene, graphdiyne and nanoribbons, it is less obvious that neglecting polaronic effects is strictly valid in organic crystals, but in general the mobilities predicted for

oligoacenes and DAcTTs using this model are in reasonable agreement with measured data.

4. Conclusions and outlook

The present review has been focused on first-principles prediction of charge mobility for carbon and organic nanomaterials, based on Boltzmann transport theory and deformation potential theory, where LA phonon scatterings are modeled by uniform lattice dilation. We calculate the charge mobilities of graphene sheet and its various 1D nanoribbons, graphdiyne sheet and 1D nanoribbons, oligoacenes, as well as DAcTTs. We found that both graphene and graphdiyne exhibit high charge mobilities, about 10^5 cm^2 V^{-1} s^{-1} and 10^4 cm^2 V^{-1} s^{-1}, respectively at room temperature. Interesting charge transport properties are predicted for the nanoribbons. For graphene nanoribbons, it is found that the polarity (electron or hole) of carriers is dependent on the ribbon width when the edge is of armchair type, where a periodicity of three is predicted: for $N = 3k$, the electron mobility at room temperature can reach 10^6 cm^2 V^{-1} s^{-1} and the hole mobility is only 10^4 cm^2 V^{-1} s^{-1}; for $N = 3k + 1$ or $3k + 2$, the hole mobility is calculated to be $\sim 5 \times 10^4$ cm^2 V^{-1} s^{-1} at room temperature, and the electron mobility is about 10^4 cm^2 V^{-1} s^{-1}. Such exotic behavior arises from the frontier orbital's bonding and anti-bonding character along the transport direction. The transport model is used based on the delocalized charged state scattered by acoustic phonon. We extend our discussion to some organic molecular crystals with close intermolecular packing structure, *i.e.*, oligoacenes and DAcTTs, where a delocalized band transport model is appropriate. It is found that the bandwidth is typically around a few tenths of an eV and the charge mobilities range from a few tens to a few hundred cm^2 V^{-1} s^{-1}. We find that the LA phonon scattering plays an important role in the charge transport of organic materials and the temperature dependence of mobilities of these organics materials satisfy the power law.[37]

We show here that the Boltzmann transport theory under the relaxation-time approximation and the LA phonon scattering modeled by DP theory are good starting points for quantitatively predicting the charge mobility through first-principles calculations, as demonstrated for the examples of the novel carbon and organic materials. The electron–phonon coupling has been modeled in a very simple way. The optical phonons and the phonon dispersion effect have been completely ignored. Impurity or disorders are not considered. We point out two directions for further improvements: (i) under the band picture, electron–phonon scatterings should be taken into account in a more sophisticated way, for instance, by employing the density functional perturbation theory with localization treatment[96] to calculate all types of phonons scattering and dispersion from first-principles. (ii) for complex system where band description is inappropriate and the electron–phonon coupling is strong, a hybrid approach combining molecular dynamics for nuclear motion and quantum mechanics for electronic structure "on the fly" with consideration of their mutual influence,[181] is expected to bridge the hopping description and the band model. In one word, modeling charge transport in organic nanomaterials at the first-principles level is a formidable task and poses great challenges in the description of electron–phonon coupling and the electron-nuclear dynamics.

Acknowledgements

This work is supported by National Natural Science Foundation of China (Grant nos. 20833004, 90921007, 20920102031) and the Ministry of Science and Technology through 973 program (Grant nos. 2009CB623600, 2011CB932304, 2011CB808405).

References

1 P. Avouris, Z. Chen and V. Perebeinos, *Nat. Nanotechnol.*, 2007, **2**, 605–615.
2 Y. Shirota and H. Kageyama, *Chem. Rev.*, 2007, **107**, 953–1010.
3 M. Burghard, H. Klauk and K. Kern, *Adv. Mater.*, 2009, **21**, 2586–2600.
4 R. A. Logan and A. J. Peters, *J. Appl. Phys.*, 1960, **31**, 122–124.
5 S. Iijima, *Nature*, 1991, **354**, 56–58.
6 K. S. Novoselov, A. K. Geim, S. V. Morozov, D. Jiang, Y. Zhang, S. V. Dubonos, I. V. Grigorieva and A. A. Firsov, *Science*, 2004, **306**, 666–669.
7 T. Dürkop, S. A. Getty, E. Cobas and M. S. Fuhrer, *Nano Lett.*, 2003, **4**, 35–39.
8 Y. Zhang, Y. Tan, H. L. Stormer and P. Kim, *Nature*, 2005, **438**, 201–204.
9 Z. Song, X. Li, X. Wu, N. Brown, C. Naud, D. Mayou, T. Li, J. Hass, A. N. Marchenkov, E. H. Conrad, P. N. First and W. A. de Heer, *Science*, 2006, **312**, 1191–1196.
10 P. Neugebauer, M. Orlita, C. Faugeras, A. L. Barra and M. Potemski, *Phys. Rev. Lett.*, 2009, **103**, 136403.
11 A. Tsumura, H. Koezuka and T. Ando, *Appl. Phys. Lett.*, 1986, **49**, 1210–1212.
12 G. Horowitz, *Adv. Mater.*, 1998, **10**, 365–377.
13 H. Yan, Z. Chen, Y. Zheng, C. Newman, J. R. Quinn, F. Dotz, M. Kastler and A. Facchetti, *Nature*, 2009, **457**, 679–686.
14 Y. Noh, N. Zhao, M. Caironi and H. Sirringhaus, *Nat. Nanotechnol.*, 2007, **2**, 784–789.
15 A. Assadi, C. Svensson, M. Willander and O. Inganas, *Appl. Phys. Lett.*, 1988, **53**, 195–197.
16 R. Madru, G. Guillaud, M. Al Sadoun, M. Maitrot, J. J. André, J. Simon and R. Even, *Chem. Phys. Lett.*, 1988, **145**, 343–346.
17 G. Horowitz, D. Fichou, X. Peng, Z. Xu and F. Garnier, *Solid State Commun.*, 1989, **72**, 381–384.
18 C. R. Newman, C. D. Frisbie, D. A. Da Silva Filho, J. Brédas, P. C. Ewbank and K. R. Mann, *Chem. Mater.*, 2004, **16**, 4436–4451.
19 V. Podzorov, E. Menard, A. Borissov, V. Kiryukhin, J. A. Rogers and M. E. Gershenson, *Phys. Rev. Lett.*, 2004, **93**, 86602.
20 O. Ostroverkhova, D. G. Cooke, F. A. Hegmann, J. E. Anthony, V. Podzorov, M. E. Gershenson, O. D. Jurchescu and T. T. M. Palstra, *Appl. Phys. Lett.*, 2006, **88**, 162101–162103.
21 O. D. Jurchescu, J. Baas and T. T. M. Palstra, *Appl. Phys. Lett.*, 2004, **84**, 3061–3063.
22 K. Nakayama, Y. Hirose, J. Soeda, M. Yoshizumi, T. Uemura, M. Uno, W. Li, M. J. Kang, M. Yamagishi, Y. Okada, E. Miyazaki, Y. Nakazawa, A. Nakao, K. Takimiya and J. Takeya, *Adv. Mater.*, 2011, **23**, 1626–1629.
23 H. Minemawari, T. Yamada, H. Matsui, J. Y. Tsutsumi, S. Haas, R. Chiba, R. Kumai and T. Hasegawa, *Nature*, 2011, **475**, 364–367.
24 G. Nan, X. Yang, L. Wang, Z. Shuai and Y. Zhao, *Phys. Rev. B: Condens. Matter Mater. Phys.*, 2009, **79**, 115203.
25 A. Troisi, *Chem. Soc. Rev.*, 2011, **40**, 2347–2358.
26 V. Coropceanu, J. Cornil, D. A. Da Silva Filho, Y. Olivier, R. Silbey and J. Brédas, *Chem. Rev.*, 2007, **107**, 926–952.
27 Z. Shuai, L. Wang and Q. Li, *Adv. Mater.*, 2011, **23**, 1145–1153.
28 H. Bässler, *Phys. Status Solidi B*, 1993, **175**, 15–56.
29 R. A. Marcus, *Rev. Mod. Phys.*, 1993, **65**, 599–610.
30 A. N. Sokolov, S. Atahan-Evrenk, R. Mondal, H. B. Akkerman, R. S. Sánchez-Carrera, S. Granados-Focil, J. Schrier, S. C. B. Mannsfeld, A. P. Zoombelt, Z. Bao and A. Aspuru-Guzik, *Nat. Commun.*, 2011, **2**, 437.
31 J. L. Brédas, J. P. Calbert, D. A. da Silva Filho and J. Cornil, *Proc. Natl. Acad. Sci. U. S. A.*, 2002, **99**, 5804.
32 Y. Song, C. Di, X. Yang, S. Li, W. Xu, Y. Liu, L. Yang, Z. Shuai, D. Zhang and D. Zhu, *J. Am. Chem. Soc.*, 2006, **128**, 15940–15941.

33 Y. C. Cheng, R. J. Silbey, D. A. D. S. Filho, J. P. Calbert, J. Cornil and J. L. Bredas, *J. Chem. Phys.*, 2003, **118**, 3764–3774.
34 W. Warta and N. Karl, *Phys. Rev. B*, 1985, **32**, 1172–1182.
35 G. D. Mahan, *Many-particle Physics*, Plenum, New York, 2nd edn, 1990.
36 (*a*) K. Hannewald and P. A. Bobbert, *Phys. Rev. B: Condens. Matter Mater. Phys.*, 2004, **69**, 75212; (*b*) L. J. Wang, Q. Peng, Q. K. Li and Z. Shuai, *J. Chem. Phys.*, 2007, **127**, 044506; (*c*) F. Ortmann and S. Roche, *Phys. Rev. B: Condens. Matter Mater. Phys.*, 2011, **84**, 180302(R).
37 L. Tang, M. Long, D. Wang and Z. Shuai, *Sci. China, Ser. B: Chem.*, 2009, **52**, 1646–1652.
38 J. Bardeen and W. Shockley, *Phys. Rev.*, 1950, **80**, 72–80.
39 L. Wang, G. Nan, X. Yang, Q. Peng, Q. Li and Z. Shuai, *Chem. Soc. Rev.*, 2010, **39**, 423–434.
40 M. E. Gershenson, V. Podzorov and A. F. Morpurgo, *Rev. Mod. Phys.*, 2006, **78**, 973–989.
41 N. Sa, G. Wang, B. Yin and Y. Huang, *Phys. E.*, 2008, **40**, 2396–2399.
42 F. B. Beleznay, F. Bogar and J. Ladik, *J. Chem. Phys.*, 2003, **119**, 5690–5695.
43 J. E. Northrup, *Appl. Phys. Lett.*, 2011, **99**, 62111–62113.
44 G. Wang and Y. Huang, *J. Phys. Chem. Solids*, 2007, **68**, 2003–2007.
45 J. M. Ziman, *Principles of the Theory of Solids*, Cambridge University, London, 2nd edn, 1972.
46 C. Jacoboni and L. Reggiani, *Rev. Mod. Phys.*, 1983, **55**, 645–705.
47 A. Akturk and N. Goldsman, *J. Appl. Phys.*, 2008, **103**, 53702–53708.
48 G. Pennington and N. Goldsman, *Phys. Rev. B: Condens. Matter*, 2003, **68**, 45426.
49 A. R. Hutson, *Phys. Rev. Lett.*, 1960, **4**, 505–507.
50 B. L. Gelmont, M. Shur and M. Stroscio, *J. Appl. Phys.*, 1995, **77**, 657–660.
51 C. Jacoboni and L. Reggiani, *Adv. Phys.*, 1979, **28**, 493–553.
52 K. Seeger, *Semiconductor Physics: An Introduction*, Springer-Verlag, Berlin, 7th edn, 1999.
53 D. Chattopadhyay and H. J. Queisser, *Rev. Mod. Phys.*, 1981, **53**, 745–768.
54 E. Conwell and V. F. Weisskopf, *Phys. Rev.*, 1950, **77**, 388–390.
55 H. Brooks, *Phys. Rev.*, 1951, **83**, 879.
56 O. D. Restrepo, K. Varga and S. T. Pantelides, *Appl. Phys. Lett.*, 2009, **94**, 212103.
57 V. Lordi, P. Erhart and D. Åberg, *Phys. Rev. B: Condens. Matter Mater. Phys.*, 2010, **81**, 235204.
58 E. H. Hwang and S. Das Sarma, *Phys. Rev. B: Condens. Matter Mater. Phys.*, 2007, **75**, 205418.
59 M. P. Persson, H. Mera, Y. Niquet, C. Delerue and M. Diarra, *Phys. Rev. B: Condens. Matter Mater. Phys.*, 2010, **82**, 115318.
60 E. H. Hwang, S. Adam and S. Das Sarma, *Phys. Rev. Lett.*, 2007, **98**, 186806.
61 T. Ando, *J. Phys. Soc. Jpn.*, 2006, **75**, 74716.
62 E. H. Hwang and S. Das Sarma, *Phys. Rev. B: Condens. Matter Mater. Phys.*, 2009, **79**, 165404.
63 L. Brey and H. A. Fertig, *Phys. Rev. B: Condens. Matter Mater. Phys.*, 2007, **75**, 125434.
64 H. Sirringhaus, *Adv. Mater.*, 2009, **21**, 3859–3873.
65 E. H. Hwang and S. Das Sarma, *Phys. Rev. B: Condens. Matter Mater. Phys.*, 2008, **77**, 115449.
66 R. S. Shishir and D. K. Ferry, *J. Phys.: Condens. Matter*, 2009, **21**, 232204.
67 K. I. Bolotin, K. J. Sikes, J. Hone, H. L. Stormer and P. Kim, *Phys. Rev. Lett.*, 2008, **101**, 96802.
68 J. H. Chen, C. Jang, M. Ishigami, S. Xiao, W. G. Cullen, E. D. Williams and M. S. Fuhrer, *Solid State Commun.*, 2009, **149**, 1080–1086.
69 X. Hong, A. Posadas, K. Zou, C. H. Ahn and J. Zhu, *Phys. Rev. Lett.*, 2009, **102**, 136808.
70 H. Fröhlich, *Phys. Rev.*, 1950, **79**, 845–856.
71 T. Holstein, *Ann. Phys.*, 1959, **8**, 343–389.
72 J. Bardeen and D. Pines, *Phys. Rev.*, 1955, **99**, 1140–1150.
73 P. B. Allen, M. L. Cohen, L. M. Falicov and R. V. Kasowski, *Phys. Rev. Lett.*, 1968, **21**, 1794–1796.
74 M. M. Dacorogna, M. L. Cohen and P. K. Lam, *Phys. Rev. Lett.*, 1985, **55**, 837–840.
75 P. K. Lam, M. M. Dacorogna and M. L. Cohen, *Phys. Rev. B*, 1986, **34**, 5065–5069.
76 S. Y. Savrasov, D. Y. Savrasov and O. K. Andersen, *Phys. Rev. Lett.*, 1994, **72**, 372–375.
77 S. Y. Savrasov and O. K. Andersen, *Phys. Rev. Lett.*, 1996, **77**, 4430–4433.
78 S. Y. Savrasov and D. Y. Savrasov, *Phys. Rev. B: Condens. Matter*, 1996, **54**, 16487–16501.
79 J. Brédas, D. Beljonne, V. Coropceanu and J. Cornil, *Chem. Rev.*, 2004, **104**, 4971–5004.
80 R. W. Munn and R. Silbey, *J. Chem. Phys.*, 1985, **83**, 1854–1864.
81 V. M. Kenkre, J. D. Andersen, D. H. Dunlap and C. B. Duke, *Phys. Rev. Lett.*, 1989, **62**, 1165–1168.
82 K. Hannewald and P. A. Bobbert, *Appl. Phys. Lett.*, 2004, **85**, 1535–1537.
83 S. Baroni, S. de Gironcoli, A. Dal Corso and P. Giannozzi, *Rev. Mod. Phys.*, 2001, **73**, 515–562.
84 P. Hohenberg and W. Kohn, *Phys. Rev.*, 1964, **136**, B864–B871.
85 W. Kohn and L. J. Sham, *Phys. Rev.*, 1965, **140**, A1133–A1138.
86 S. Piscanec, M. Lazzeri, F. Mauri, A. C. Ferrari and J. Robertson, *Phys. Rev. Lett.*, 2004, **93**, 185503.
87 J. Yan, W. Y. Ruan and M. Y. Chou, *Phys. Rev. B: Condens. Matter Mater. Phys.*, 2008, **77**, 125401.
88 G. Zheng, S. J. Clark, P. R. Tulip, S. Brand and R. A. Abram, *J. Chem. Phys.*, 2005, **123**, 24904–24908.
89 L. Boeri, O. V. Dolgov and A. A. Golubov, *Phys. Rev. Lett.*, 2008, **101**, 26403.
90 L. Xu, Y. Zheng and J. Zheng, *Phys. Rev. B: Condens. Matter Mater. Phys.*, 2010, **82**, 195102.
91 J. Sjakste, N. Vast and V. Tyuterev, *Phys. Rev. Lett.*, 2007, **99**, 236405.
92 K. M. Borysenko, J. T. Mullen, E. A. Barry, S. Paul, Y. G. Semenov, J. M. Zavada, M. B. Nardelli and K. W. Kim, *Phys. Rev. B: Condens. Matter Mater. Phys.*, 2010, **81**, 121412.
93 K. M. Borysenko, J. T. Mullen, X. Li, Y. G. Semenov, J. M. Zavada, M. B. Nardelli and K. W. Kim, *Phys. Rev. B: Condens. Matter Mater. Phys.*, 2011, **83**, 161402.
94 M. J. Verstraete and X. Gonze, *Phys. Rev. B: Condens. Matter Mater. Phys.*, 2006, **74**, 153408.
95 A. Subedi and L. Boeri, *Phys. Rev. B: Condens. Matter Mater. Phys.*, 2011, **84**, 20508.
96 F. Giustino, M. L. Cohen and S. G. Louie, *Phys. Rev. B: Condens. Matter Mater. Phys.*, 2007, **76**, 165108.
97 J. Noffsinger, F. Giustino, S. G. Louie and M. L. Cohen, *Phys. Rev. B: Condens. Matter Mater. Phys.*, 2009, **79**, 104511.
98 T. Bazhirov, J. Noffsinger and M. L. Cohen, *Phys. Rev. B: Condens. Matter Mater. Phys.*, 2011, **84**, 125122.
99 M. Casula, M. Calandra, G. Profeta and F. Mauri, *Phys. Rev. Lett.*, 2011, **107**, 137006.
100 N. Vukmirović and L. Wang, *J. Chem. Phys.*, 2008, **128**, 121102–121104.
101 N. Vukmirović and L. Wang, *J. Phys. Chem. B*, 2008, **113**, 409–415.
102 N. Vukmirović and L. Wang, *Nano Lett.*, 2009, **9**, 3996–4000.
103 M. Long, L. Tang, D. Wang, L. Wang and Z. Shuai, *J. Am. Chem. Soc.*, 2009, **131**, 17728–17729.
104 M. Long, L. Tang, D. Wang, Y. Li and Z. Shuai, *ACS Nano*, 2011, **5**, 2593–2600.
105 W. A. Harrison, *Phys. Rev.*, 1956, **104**, 1281–1290.
106 W. Walukiewicz, H. E. Ruda, J. Lagowski and H. C. Gatos, *Phys. Rev. B*, 1984, **30**, 4571–4582.
107 S. Takagi, J. L. Hoyt, J. J. Welser and J. F. Gibbons, *J. Appl. Phys.*, 1996, **80**, 1567–1577.
108 P. J. Price, *Ann. Phys.*, 1981, **133**, 217–239.
109 B. Xu, Y. D. Xia, J. Yin, X. G. Wan, K. Jiang, A. D. Li, D. Wu and Z. G. Liu, *Appl. Phys. Lett.*, 2010, **96**, 183103–183108.
110 G. K. H. Madsen and D. J. Singh, *Comput. Phys. Commun.*, 2006, **175**, 67–71.
111 S. Wei and A. Zunger, *Phys. Rev. B: Condens. Matter*, 1999, **60**, 5404–5411.
112 M. Cardona and N. E. Christensen, *Phys. Rev. B*, 1987, **35**, 6182–6194.
113 C. G. Van de Walle, *Phys. Rev. B*, 1989, **39**, 1871–1883.
114 O. L. Lazarenkova, P. von Allmen, F. Oyafuso, S. Lee and G. Klimeck, *Appl. Phys. Lett.*, 2004, **85**, 4193–4195.

115 A. J. Williamson, L. W. Wang and A. Zunger, *Phys. Rev. B: Condens. Matter*, 2000, **62**, 12963–12977.
116 G. Kresse and J. Hafner, *Phys. Rev. B: Condens. Matter*, 1993, **47**, 558–561.
117 G. Kresse and J. Hafner, *Phys. Rev. B: Condens. Matter*, 1994, **49**, 14251–14269.
118 G. Kresse and J. Furthmüller, *Comput. Mater. Sci.*, 1996, **6**, 15–50.
119 G. Kresse and J. Furthmüller, *Phys. Rev. B: Condens. Matter*, 1996, **54**, 11169–11186.
120 G. Kresse and D. Joubert, *Phys. Rev. B: Condens. Matter Mater. Phys.*, 1999, **59**, 1758–1775.
121 S. Das Sarma, S. Adam, E. H. Hwang and E. Rossi, *Rev. Mod. Phys.*, 2011, **83**, 407–470.
122 A. H. Castro Neto, F. Guinea, N. M. R. Peres, K. S. Novoselov and A. K. Geim, *Rev. Mod. Phys.*, 2009, **81**, 109–162.
123 M. Sprinkle, M. Ruan, Y. Hu, J. Hankinson, M. Rubio-Roy, B. Zhang, X. Wu, C. Berger and W. A. de Heer, *Nat. Nanotechnol.*, 2010, **5**, 727–731.
124 Y. Shin, J. Y. Son, M. Jo, Y. Shin and H. M. Jang, *J. Am. Chem. Soc.*, 2011, **133**, 5623–5625.
125 M. Y. Han, B. Özyilmaz, Y. Zhang and P. Kim, *Phys. Rev. Lett.*, 2007, **98**, 206805.
126 X. Wang, Y. Ouyang, X. Li, H. Wang, J. Guo and H. Dai, *Phys. Rev. Lett.*, 2008, **100**, 206803.
127 F. Chen, Q. Qing, J. Xia, J. Li and N. Tao, *J. Am. Chem. Soc.*, 2009, **131**, 9908–9909.
128 J. S. Bunch, A. M. van der Zande, S. S. Verbridge, I. W. Frank, D. M. Tanenbaum, J. M. Parpia, H. G. Craighead and P. L. McEuen, *Science*, 2007, **315**, 490–493.
129 S. Latil and L. Henrard, *Phys. Rev. Lett.*, 2006, **97**, 36803.
130 H. Bai, Y. Zhu, W. Qiao and Y. Huang, *RSC Adv.*, 2011, **1**, 768–775.
131 F. Ricardo and A. Pablo, *J. Phys.: Condens. Matter*, 2009, **21**, 285304.
132 K. T. Chan, J. B. Neaton and M. L. Cohen, *Phys. Rev. B: Condens. Matter Mater. Phys.*, 2008, **77**, 235430.
133 J. P. Perdew, K. Burke and M. Ernzerhof, *Phys. Rev. Lett.*, 1996, **77**, 3865–3868.
134 L. A. Burns, A. V. Mayagoitia, B. G. Sumpter and C. D. Sherrill, *J. Chem. Phys.*, 2011, **134**, 84107–84125.
135 S. Grimme, *J. Comput. Chem.*, 2006, **27**, 1787–1799.
136 V. Barone, M. Casarin, D. Forrer, M. Pavone, M. Sambi and A. Vittadini, *J. Comput. Chem.*, 2009, **30**, 934–939.
137 H. J. Monkhorst and J. D. Pack, *Phys. Rev. B: Solid State*, 1976, **13**, 5188–5192.
138 P. Trucano and R. Chen, *Nature*, 1975, **258**, 136–137.
139 P. V. Avramov, S. Sakai, S. Entani, Y. Matsumoto and H. Naramoto, *Chem. Phys. Lett.*, 2011, **508**, 86–89.
140 I. V. Lebedeva, A. A. Knizhnik, A. M. Popov, Y. E. Lozovik and B. V. Potapkin, *Phys. Chem. Chem. Phys.*, 2011, **13**, 5687–5695.
141 K. I. Bolotin, K. J. Sikes, Z. Jiang, M. Klima, G. Fudenberg, J. Hone, P. Kim and H. L. Stormer, *Solid State Commun.*, 2008, **146**, 351–355.
142 H. Min, B. Sahu, S. K. Banerjee and A. H. MacDonald, *Phys. Rev. B: Condens. Matter Mater. Phys.*, 2007, **75**, 155115.
143 S. V. Morozov, K. S. Novoselov, M. I. Katsnelson, F. Schedin, D. C. Elias, J. A. Jaszczak and A. K. Geim, *Phys. Rev. Lett.*, 2008, **100**, 16602.
144 S. Xiao, J. Chen, S. Adam, E. D. Williams and M. S. Fuhrer, *Phys. Rev. B: Condens. Matter Mater. Phys.*, 2010, **82**, 41406.
145 X. Li, K. M. Borysenko, M. B. Nardelli and K. W. Kim, *Phys. Rev. B: Condens. Matter Mater. Phys.*, 2011, **84**, 195453.
146 K. Nagashio, T. Nishimura, K. Kita and A. Toriumi, *Appl. Phys. Express*, 2009, **2**, 25001–25003.
147 Y. Kopelevich and P. Esquinazi, *Adv. Mater.*, 2007, **19**, 4559–4563.
148 X. Li, X. Wang, L. Zhang, S. Lee and H. Dai, *Science*, 2008, **319**, 1229–1232.
149 L. Brey and H. A. Fertig, *Phys. Rev. B: Condens. Matter Mater. Phys.*, 2006, **73**, 235411.
150 Y. Son, M. L. Cohen and S. G. Louie, *Phys. Rev. Lett.*, 2006, **97**, 216803.
151 H. Raza and E. C. Kan, *Phys. Rev. B: Condens. Matter Mater. Phys.*, 2008, **77**, 245434.
152 H. W. Kroto, J. R. Heath, S. C. O'Brien, R. F. Curl and R. E. Smalley, *Nature*, 1985, **318**, 162–163.
153 R. H. Baughman, H. Eckhardt and M. Kertesz, *J. Chem. Phys.*, 1987, **87**, 6687–6699.
154 M. M. Haley, S. C. Brand and J. J. Pak, *Angew. Chem., Int. Ed. Engl.*, 1997, **36**, 836–838.
155 M. M. Haley and W. B. Wan, in *Advances in Strained and Interesting Organic Molecules*, ed. B. Halton, 2000, vol. 8, pp. 1–41.
156 G. Li, Y. Li, H. Liu, Y. Guo, Y. Li and D. Zhu, *Chem. Commun.*, 2010, **46**, 3256–3258.
157 C. Li, J. Li, F. Wu, S. Li, J. Xia and L. Wang, *J. Phys. Chem. C*, 2011, **115**, 23221–23225.
158 G. Luo, X. Qian, H. Liu, R. Qin, J. Zhou, L. Li, Z. Gao, E. Wang, W. Mei, J. Lu, Y. Li and S. Nagase, *Phys. Rev. B: Condens. Matter Mater. Phys.*, 2011, **84**, 75439.
159 N. Narita, S. Nagai, S. Suzuki and K. Nakao, *Phys. Rev. B: Condens. Matter*, 1998, **58**, 11009–11014.
160 N. Narita, S. Nagai and S. Suzuki, *Phys. Rev. B: Condens. Matter*, 2001, **64**, 245408.
161 M. Kondo, D. Nozaki, M. Tachibana, T. Yumura and K. Yoshizawa, *Chem. Phys.*, 2005, **312**, 289–297.
162 K. Takimiya, S. Shinamura, I. Osaka and E. Miyazaki, *Adv. Mater.*, 2011, **23**, 4347–4370.
163 J. E. Northrup, *Phys. Rev. B: Condens. Matter Mater. Phys.*, 2007, **76**, 245202.
164 K. Hummer, P. Puschnig and C. Ambrosch-Draxl, *Phys. Rev. B: Condens. Matter*, 2003, **67**, 184105.
165 V. I. Ponomarev, O. S. Filipenko and L. O. Atovmyan, *Kristallografiya*, 1976, **21**, 392–394.
166 C. P. Brock and J. D. Dunitz, *Acta Crystallogr., Sect. B: Struct. Sci.*, 1990, **46**, 795–806.
167 D. Holmes, S. Kumaraswamy, A. J. Matzger and K. P. C. Vollhardt, *Chem.–Eur. J.*, 1999, **5**, 3399–3412.
168 G. K. Afanasev, *Sov. Phys. Crystallogr.*, 1969, **13**, 892.
169 N. Karl, *Synth. Met.*, 2003, **133–134**, 649–657.
170 R. W. I. de Boer, M. E. Gershenson, A. F. Morpurgo and V. Podzorov, *Phys. Status Solidi A*, 2004, **201**, 1302–1331.
171 R. G. Kepler, *Phys. Rev.*, 1960, **119**, 1226–1229.
172 C. Liu, T. Minari, X. Lu, A. Kumatani, K. Takimiya and K. Tsukagoshi, *Adv. Mater.*, 2011, **23**, 523–526.
173 T. Izawa, E. Miyazaki and K. Takimiya, *Adv. Mater.*, 2008, **20**, 3388–3392.
174 M. Uno, Y. Tominari, M. Yamagishi, I. Doi, E. Miyazaki, K. Takimiya and J. Takeya, *Appl. Phys. Lett.*, 2009, **94**, 223303–223308.
175 S. Haas, Y. Takahashi, K. Takimiya and T. Hasegawa, *Appl. Phys. Lett.*, 2009, **95**, 22111–22113.
176 K. Niimi, S. Shinamura, I. Osaka, E. Miyazaki and K. Takimiya, *J. Am. Chem. Soc.*, 2011, **133**, 8732–8739.
177 R. S. Sánchez-Carrera, S. Atahan, J. Schrier and A. Aspuru-Guzik, *J. Phys. Chem. C*, 2010, **114**, 2334–2340.
178 T. Yamamoto and K. Takimiya, *J. Am. Chem. Soc.*, 2007, **129**, 2224–2225.
179 R. S. Sánchez-Carrera, P. Paramonov, G. M. Day, V. Coropceanu and J. Brédas, *J. Am. Chem. Soc.*, 2010, **132**, 14437–14446.
180 F. Valiyev, W. Hu, H. Chen, M. Kuo, I. Chao and Y. Tao, *Chem. Mater.*, 2007, **19**, 3018–3026.
181 L. Wang, D. Beljonne, L. Chen and Q. Shi, *J. Chem. Phys.*, 2011, **134**, 244116–244118.